Technical Design Report for the

$\overline{\text{P}}$ANDA

(AntiProton Annihilations at Darmstadt)

Strong Interaction Studies with Antiprotons

Cluster-Jet and Pellet Targets

$\overline{\text{P}}$ANDA Collaboration

Draft Copy, Revision 44, February 16, 2009

This document forms part of the $\overline{\text{P}}$ANDA Technical Design Report and covers the cluster-jet and the pellet targets.

The $\overline{\text{P}}$ANDA Collaboration

Universität **Basel**, Switzerland
W. Erni, I. Keshelashvili, B. Krusche, M. Steinacher

Institute of High Energy Physics, Chinese Academy of Sciences, **Beijing**, China
Y. Heng, Z. Liu, H. Liu, X. Shen, O. Wang, H. Xu

Ruhr-Universität **Bochum**, Institut für Experimentalphysik I, Germany
J. Becker, F. Feldbauer, F.-H. Heinsius, T. Held, H. Koch, B. Kopf, M. Pelizäus, T. Schröder, M. Steinke, U. Wiedner, J. Zhong

Università di **Brescia**, Italy
A. Bianconi

Institutul National de C&D pentru Fizica si Inginerie Nucleara "Horia Hulubei", **Bukarest-Magurele**, Romania
M. Bragadireanu, D. Pantea, A. Tudorache, V. Tudorache

Dipartimento di Fisica e Astronomia dell'Università di **Catania** and INFN, Sezione di **Catania**, Italy
M. De Napoli, F. Giacoppo, G. Raciti, E. Rapisarda, C. Sfienti

IFJ, Institute of Nuclear Physics PAN, **Cracow**, Poland
E. Bialkowski, A. Budzanowski, B. Czech, M. Kistryn, S. Kliczewski, A. Kozela, P. Kulessa, K. Pysz, W. Schäfer, R. Siudak, A. Szczurek

Institute of Applied Informatics, **Cracow** University of Technology, Poland
W. Czyżycki, M. Domagała, M. Hawryluk, E. Lisowski, F. Lisowski, L. Wojnar

Institute of Physics, Jagiellonian University, **Cracow**, Poland
D. Gil, P. Hawranek, B. Kamys, St. Kistryn, K. Korcyl, W. Krzemień, A. Magiera, P. Moskal, Z. Rudy, P. Salabura, J. Smyrski, A. Wrońska

GSI Helmholtzzentrum für Schwerionenforschung GmbH, **Darmstadt**, Germany
M. Al-Turany, I. Augustin, H. Deppe, H. Flemming, J. Gerl, K. Götzen, R. Hohler, D. Lehmann, B. Lewandowski, J. Lühning, F. Maas, D. Mishra, H. Orth, K. Peters, T. Saito, G. Schepers, C.J. Schmidt, L. Schmitt, C. Schwarz, B. Voss, P. Wieczorek, A. Wilms

Technische Universität **Dresden**, Germany
K.-T. Brinkmann, H. Freiesleben, R. Jäkel, R. Kliemt, T. Würschig, H.-G. Zaunick

Veksler-Baldin Laboratory of High Energies (VBLHE), Joint Institute for Nuclear Research, **Dubna**, Russia
V.M. Abazov, G. Alexeev, A. Arefiev, V.I. Astakhov, M.Yu. Barabanov, B.V. Batyunya, Yu.I. Davydov, V.Kh. Dodokhov, A.A. Efremov, A.G. Fedunov, A.A. Feshchenko, A.S. Galoyan, S. Grigoryan, A. Karmokov, E.K. Koshurnikov, V.Ch. Kudaev, V.I. Lobanov, Yu.Yu. Lobanov, A.F. Makarov, L.V. Malinina, V.L. Malyshev, G.A. Mustafaev, A. Olshevski, M.A.. Pasyuk, E.A. Perevalova, A.A. Piskun, T.A. Pocheptsov, G. Pontecorvo, V.K. Rodionov, Yu.N. Rogov, R.A. Salmin, A.G. Samartsev, M.G. Sapozhnikov, A. Shabratova, G.S. Shabratova, A.N. Skachkova, N.B. Skachkov, E.A. Strokovsky, M.K. Suleimanov, R.Sh. Teshev, V.V. Tokmenin, V.V. Uzhinsky A.S. Vodopianov, S.A. Zaporozhets, N.I. Zhuravlev, A.G. Zorin

University of **Edinburgh**, United Kingdom
D. Branford, K. Föhl, D. Glazier, D. Watts, P. Woods

Friedrich Alexander Universität **Erlangen-Nürnberg**, Germany
W. Eyrich, A. Lehmann, A. Teufel

Northwestern University, **Evanston**, U.S.A.
S. Dobbs, Z. Metreveli, K. Seth, B. Tann, A. Tomaradze

Università di **Ferrara** and INFN, Sezione di **Ferrara**, Italy
D. Bettoni, V. Carassiti, A. Cecchi, P. Dalpiaz, E. Fioravanti, I. Garzia, M. Negrini, M. Savriè, G. Stancari

INFN-Laboratori Nazionali di **Frascati**, Italy
B. Dulach, P. Gianotti, C. Guaraldo, V. Lucherini, E. Pace

INFN, Sezione di **Genova**, Italy
A. Bersani, M. Macri, M. Marinelli, R.F. Parodi

Justus Liebig-Universität **Gießen**, II. Physikalisches Institut, Germany
I. Brodski, W. Döring, P. Drexler, M. Düren, Z. Gagyi-Palffy, A. Hayrapetyan, M. Kotulla, W. Kühn, S. Lange, M. Liu, V. Metag, M. Nanova, R. Novotny, C. Salz, J. Schneider, P. Schönmeier, R. Schubert, S. Spataro, H. Stenzel, C. Strackbein, M. Thiel, U. Thöring, S. Yang,

University of **Glasgow**, United Kingdom
T. Clarkson, E. Cowie, E. Downie, G. Hill, M. Hoek, D. Ireland, R. Kaiser, T. Keri, I. Lehmann, K. Livingston, S. Lumsden, D. MacGregor, B. McKinnon, M. Murray, D. Protopopescu, G. Rosner, B. Seitz, G. Yang

Kernfysisch Versneller Instituut, University of **Groningen**, Netherlands
M. Babai, A.K. Biegun, A. Bubak, E. Guliyev, V.S. Jothi, M. Kavatsyuk, H. Löhner, J. Messchendorp, H. Smit, J.C. van der Weele

Helsinki Institute of Physics, Finland
F. Garcia, D.-O. Riska

Forschungszentrum **Jülich**, Jülich Center for Hadron Physics, Germany
M. Büscher, R. Dosdall, R. Dzhygadlo, A. Gillitzer, D. Grunwald, V. Jha, G. Kemmerling, H. Kleines, A. Lehrach, R. Maier, M. Mertens, H. Ohm, D. Prasuhn, T. Randriamalala, J. Ritman, M. Röder, T. Stockmanns, P. Wintz, P. Wüstner

University of Silesia, **Katowice**, Poland
J. Kisiel

Chinese Academy of Science, Institute of Modern Physics, **Lanzhou**, China
S. Li, Z. Li, Z. Sun, H. Xu

Lunds Universitet, Department of Physics, **Lund**, Sweden
S. Fissum, K. Hansen, L. Isaksson, M. Lundin, B. Schröder

Johannes Gutenberg-Universität, Institut für Kernphysik, **Mainz**, Germany
P. Achenbach, M.C. Mora Espi, J. Pochodzalla, S. Sanchez, A. Sanchez-Lorente

Research Institute for Nuclear Problems, Belarus State University, **Minsk**, Belarus
V.I. Dormenev, A.A. Fedorov, M.V. Korzhik, O.V. Missevitch

Institute for Theoretical and Experimental Physics, **Moscow**, Russia
V. Balanutsa, V. Chernetsky, A. Demekhin, A. Dolgolenko, P. Fedorets, A. Gerasimov, V. Goryachev

Moscow Power Engineering Institute, Russia
A. Boukharov, O. Malyshev, I. Marishev, A. Semenov

Technische Universität **München**, Germany
C. Höppner, B. Ketzer, I. Konorov, A. Mann, S. Neubert, S. Paul, Q. Weitzel

Westfälische Wilhelms-Universität **Münster**, Germany
A. Khoukaz, T. Rausmann, A. Täschner, J. Wessels

IIT Bombay, Department of Physics, **Mumbai**, India
R. Varma

Budker Institute of Nuclear Physics, **Novosibirsk**, Russia
E. Baldin, K. Kotov, S. Peleganchuk, Yu. Tikhonov

Institut de Physique Nucléaire, **Orsay**, France
J. Boucher, T. Hennino, R. Kunne, S. Ong, J. Pouthas, B. Ramstein, P. Rosier, M. Sudol, J. Van de Wiele, T. Zerguerras

Warsaw University of Technology, Institute of Atomic Energy, **Otwock-Swierk**, Poland
K. Dmowski, R. Korzeniewski, D. Przemyslaw, B. Slowinski

Dipartimento di Fisica Nucleare e Teorica, Università di **Pavia**, INFN, Sezione di **Pavia**, Italy
G. Boca, A. Braghieri, S. Costanza, A. Fontana, P. Genova, L. Lavezzi, P. Montagna, A. Rotondi

Institute for High Energy Physics, **Protvino**, Russia
N.I. Belikov, A.M. Davidenko, A.A. Derevschikov, Y.M. Goncharenko, V.N. Grishin, V.A. Kachanov, D.A. Konstantinov, V.A. Kormilitsin, V.I. Kravtsov, Y.A. Matulenko, Y.M. Melnik A.P. Meschanin, N.G. Minaev, V.V. Mochalov, D.A. Morozov, L.V. Nogach, S.B. Nurushev, A.V. Ryazantsev, P.A. Semenov, L.F. Soloviev, A.V. Uzunian, A.N. Vasiliev, A.E. Yakutin

Kungliga Tekniska Högskolan, **Stockholm**, Sweden
T. Bäck, B. Cederwall

Stockholms Universitet, **Stockholm**, Sweden
C. Bargholtz, L. Gerén, P.E. Tegnér

Petersburg Nuclear Physics Institute of Academy of Science, Gatchina, **St. Petersburg**, Russia
S. Belostotski, G. Gavrilov, A. Itzotov, A. Kisselev, P. Kravchenko, S. Manaenkov, O. Miklukho, Y. Naryshkin, D. Veretennikov, V. Vikhrov, A. Zhadanov

Università del Piemonte Orientale Alessandria and INFN, Sezione di **Torino**, Italy
L. Fava, D. Panzieri

Università di **Torino** and INFN, Sezione di **Torino**, Italy
D. Alberto, A. Amoroso, E. Botta, T. Bressani, S. Bufalino, M.P. Bussa, L. Busso, F. De Mori, M. Destefanis, L. Ferrero, A. Grasso, M. Greco, T. Kugathasan, M. Maggiora, S. Marcello, G. Serbanut, S. Sosio

INFN, Sezione di **Torino**, Italy
R. Bertini, D. Calvo, S. Coli, P. De Remigis, A. Feliciello, A. Filippi, G. Giraudo, G. Mazza, A. Rivetti, K. Szymanska, F. Tosello, R. Wheadon

INAF-IFSI and INFN, Sezione di **Torino**, Italy
O. Morra

Politecnico di **Torino** and INFN, Sezione di **Torino**, Italy
M. Agnello, F. Iazzi, K. Szymanska

Università di **Trieste** and INFN, Sezione di **Trieste**, Italy
R. Birsa, F. Bradamante, A. Bressan, A. Martin

Universität **Tübingen**, Germany
H. Clement

The Svedberg Laboratory, **Uppsala**, Sweden
C. Ekström

Uppsala University, Department of Physics and Astronomy, Sweden
H. Calén, S. Grape, B. Höistad, T. Johansson, A. Kupsc, P. Marciniewski, E. Thomé, J. Zlomanczuk

Universitat de **Valencia**, Dpto. de Física Atómica, Molecular y Nuclear, Spain
J. Díaz, A. Ortiz

Soltan Institute for Nuclear Studies, **Warsaw**, Poland
S. Borsuk, A. Chlopik, Z. Guzik, J. Kopec, T. Kozlowski, D. Melnychuk, M. Plominski, J. Szewinski, K. Traczyk, B. Zwieglinski

Österreichische Akademie der Wissenschaften, Stefan Meyer Institut für Subatomare Physik, **Vienna**, Austria
P. Bühler, A. Gruber, P. Kienle, J. Marton, E. Widmann, J. Zmeskal

Contents

Executive Summary

COMMENT: Author: A. Khoukaz, H. Orth, M. Büscher

basis will be the EMC part...

1 Introduction

COMMENT: Author: H. Orth

COMMENT: added the "intro" from the magnet TDR by AB

The physics of strong interactions is undoubtedly one of the most challenging areas of modern science. Quantum Chromo Dynamics (QCD) is reproducing the physics phenomena only at distances much shorter than the size of the nucleon, where perturbation theory can be used yielding results of high precision and predictive power. As the coupling constant rises steeply at nuclear scales (see Fig. 1.1) perturbative expansions diverge and a different theoretical approach is required. However, the strong interaction keeps providing new experimental observations, which were not predicted by "effective" theories. The latter retain the fundamental symmetries of QCD, but have problems in describing all the observed phenomena simultaneously.

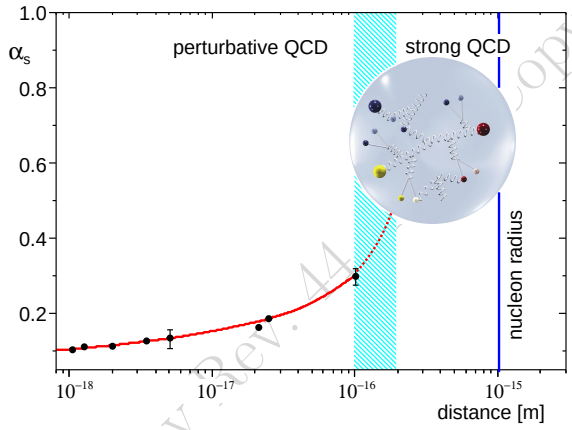

Figure 1.1: Coupling constant of the strong interaction as a function of distance. The data points represent experimental values [**?**]. For distances between quarks comparable to the nucleon size the interaction becomes so strong that quarks cannot be further separated (confinement) and hadrons are formed. $\overline{\text{P}}$ANDA will investigate the properties of the strong interaction in this key region for the understanding of matter.

The physics of strange and charmed quarks holds the potential to connect the two different energy domains interpolating between the limiting scales of QCD. In this regime only scarce experimental data is available, most of which has been obtained with electromagnetic probes.

One possible single issue that may greatly advance our understanding of hadronic structure is the predicted existence of states outside of the two- and three-quark classifications, which for example could arise from the excitation of gluonic degrees of freedom. Recent findings from running experiments at B-factories (see *e.g.* Refs [**?**, **?**]) show that, indeed, unexpected narrow states unaccounted for in the naïve quark models exist. Experiments focussed on the abundant production and systematic studies of these states are needed. Preferably, these should be performed using hadronic probes because the cross sections are expected to be very large in such systems. Results of high statistical precision are a decisive element to be able to identify and extract features of these exotic states. Hadron beams are advantageous also for the production of hadrons with non-exotic quantum numbers, as these can be formed directly with high cross sections. Phase space cooling of the antiproton beam furthermore allows high precision determination of the mass and width of such states. Using heavier nuclei as targets enables us to investigate in-medium properties of hadrons and to produce hypernuclei, even those containing more than one strange quark, copiously.

The $\overline{\text{P}}$ANDA (Antiproton Annnihilation at Darmstadt) experiment (see also Sec. 2 and Refs. [**?**, **?**]), which will be installed at the High Energy Storage Ring for antiprotons of the upcoming Facility for Antiproton and Ion Research (FAIR) [**?**], features a scientific programme devoted to the following key areas.

- Charmonium spectroscopy.
- Exotic hadrons (hybrids, glueballs, multi-quark states).
- Open and hidden charm in nuclei.
- γ-ray spectroscopy of hypernuclei.
- Hadron properties in the nuclear medium.
- Structure of the nucleon.

Selected other topics will be studied with unprecedented accuracy.

1.1 Topics Addressed at PANDA

In the following major physics topics are briefly introduced. See also Fig. 1.2 for an overview. A detailed discussion can be found in Ref. [?].

Charmonium Spectroscopy. The $c\bar{c}$ spectrum is often referred to as the positronium of QCD, because the properties of the states can be calculated precisely within the framework of non-relativistic potential models [?]. More recently, results from quenched Lattice QCD emerged describing the known spectrum rather well [?]. Recent findings of states around 4 GeV/c (X(3872), Z(3931), X(3940), Y(3940), Y(4260), Y(4320), to name only a few) [?, ?, ?, ?] show that the spectrum, which was believed to be well understood, in fact yields much more than has been expected.

PANDA will not only be able to measure those states in a different production channel, which may reveal more unexpected states, but also allow for scans over the width of those states with a precision of 10^{-5} relative to its mass. At full luminosity PANDA will be able to collect several thousand $c\bar{c}$ states per day. Thus properties and branching ratios will be determined to a unprecedented precision.

Search for Gluonic Excitations (Hybrids and Glueballs). One of the main challenges of hadron physics is the search for gluonic excitations, *i.e.* hadrons in which the gluons can act as principal components. In other words, the state cannot be fully described in terms of quantum numbers by solely taking its valence-quark content into account. These gluonic hadrons fall into two main categories described in the following. Glueballs are states where only gluons contribute to the quantum numbers while hybrids consist of a valence $q\bar{q}$ pair and one or more gluons which contribute to the overall quantum numbers.

The additional degrees of freedom carried by gluons allow these hybrids and glueballs to have J^{PC} exotic quantum numbers. In this case mixing effects with nearby $q\bar{q}$ states are excluded and this makes their experimental identification easier. The properties of glueballs and hybrids are determined by the long-distance features of QCD and their study will yield fundamental insight into the structure of the QCD vacuum. Antiproton-proton annihilations provide a very favourable environment to search for gluonic hadrons.

Multi-Quark States. These are states which cannot be assigned to an arrangement of tree quarks or a quark-antiquark pair as the classical baryons and mesons. Similarly to the gluonic excitations mentioned above they would show up as states outnumbering the multiplets and their clearest signature would be possible exotic quantum numbers. They could be interpreted as hadronic molecules or octet couplings. The well known states $a_0(980)$ and $f_0(975)$ are suspected to have admixtures of $K\bar{K}$ components. Here, however, mixing is large and clear statements on their nature are difficult to draw. In the charmonium region all states are narrower and positive identification is much more likely. This can also be seen from the current discussion on the nature of the X(3872) and other states recently found at the B-factories [?, ?].

Open and Hidden Charm in Nuclei. The study of medium modifications of hadrons embedded in hadronic matter is aimed at understanding the origin of hadron masses in the context of spontaneous chiral symmetry breaking in QCD and its partial restoration in a hadronic environment [?]. So far experiments have been focussed on the light quark sector. The high-intensity $\bar{p}$ beam of up to 15 GeV/c will allow an extension of this program to the charm sector both for hadrons with hidden and open charm. The in-medium masses of these states are expected to be affected primarily by the gluon condensate.

Another study which can be carried out in PANDA is the measurement of J/ψ and D meson production cross sections in $\bar{p}$ annihilation on a series of nuclear targets. The comparison of the resonant J/ψ yield obtained from $\bar{p}$ annihilation on protons and different nuclear targets allows to deduce the J/ψ-nucleus dissociation cross section, a fundamental parameter to understand J/ψ suppression in relativistic heavy ion collisions interpreted as a signal for quark-gluon plasma formation.

Open charm spectroscopy. The HESR running at full luminosity and at $\bar{p}$ momenta larger than 6.4 GeV/c would produce a large number of D meson pairs. The high yield (*e.g.* up to 100 charm pairs per second around the $\psi(4040)$) and the well defined production kinematics of D meson pairs would allow to carry out a significant charmed meson spectroscopy program which would include, for example, the rich D and D_s meson spectra.

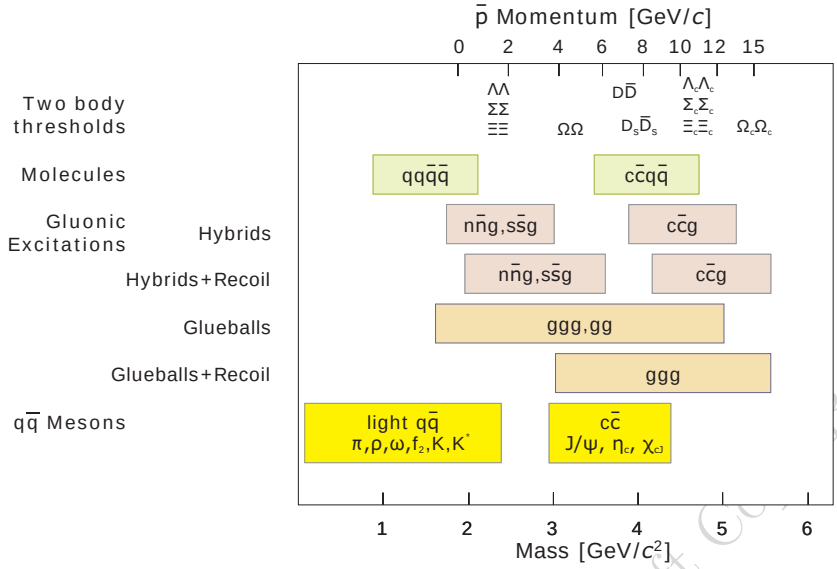

Figure 1.2: Mass range of hadrons that will be accessible at PANDA. The upper scale indicates the corresponding antiproton momenta required in a fixed-target experiment. The HESR will provide 1.5 to 15 GeV/c antiprotons, which will allow charmonium spectroscopy, the search for charmed hybrids and glueballs, the production of D meson baryon pairs for pairs and the production of hypernuclear studies.

Hypernuclear physics. Hypernuclei are systems in which up or down quarks are replaced by strange quarks. In this way a new quantum number, strangeness, is introduced into the nucleus. Although single and double Λ-hypernuclei were discovered many decades ago, only 6 events of double Λ-hypernuclei were observed up to now. The availability of $\overline{\mathrm{p}}$ beams at FAIR will allow efficient production of hypernuclei with more than one strange hadron, making PANDA competitive with planned dedicated facilities. This will open new perspectives for nuclear structure spectroscopy and for studying the hyperon-nucleon and in particular the hyperon-hyperon interaction.

Electromagnetic Processes. In addition to the spectroscopic studies described above, PANDA will be able to investigate the structure of the nucleon using electromagnetic processes, such as Wide Angle Compton Scattering (WACS) and the process $\overline{\mathrm{p}}\mathrm{p} \to e^+e^-$, which will allow the determination of the electromagnetic form factors of the proton in the timelike region over an extended q^2 region. In addition the Drell-Yan process allows to access the transverse nucleon spin structure.

1.2 Experimental Approach

Conventional as well as exotic hadrons can be produced by a range of different experimental means. Among these, hadronic annihilation processes, and in particular antiproton-nucleon and antiproton-nucleus annihilations, have proven to possess all the necessary ingredients for fruitful harvests in the hadron field.

- Hadron annihilations produce a gluon-rich environment, a fundamental prerequisite to copiously produce gluonic excitations.
- The use of antiprotons permits to directly form all states with non-exotic quantum numbers (formation experiments). Ambiguities in the reconstruction are reduced and cross sections are considerably higher compared to producing additional particles in the final state (production experiments). The appearance of states in production but not in formation is a clear sign of exotic physics.
- Narrow resonances, such as charmonium states, can be scanned with high precision in formation experiments using the small energy spread available with antiproton beams (cooled to $\Delta p/p = 10^{-5}$).
- Since exotic systems will appear only in production experiments the physics analysis of

Dalitz plots becomes important. This requires high-statistics data samples. Thus, high luminosity is a key requirement. This can be achieved using an internal target of high density, large numbers of projectiles and a high count-rate capability of the detector. The latter is mandatory since the overall cross sections of hadronic reactions are large while the cross sections of reaction channels of interest may be quite small.

- As reaction products are peaked around angles of 0° a fixed-target experiment with a magnetic spectrometer is the ideal tool. At the same time a 4π coverage is mandatory to be able to study exclusive reactions with many decay particles. The physics topics as summarised in Fig. 1.2 imply that the momentum range of the antiproton beam should extend up to 15 GeV/c with luminosities in the order of $10^{32}\,\mathrm{cm}^{-2}\mathrm{s}^{-1}$

To take full advantage of the HESR beam features, a compact, high resolution and high angular coverage spectrometer was designed. To cope with the need of 2 Tm bending power both at a very wide angular range in the laboratory reference frame, two magnets are necessary. A solenoid magnet provides the required bending power for particles exiting at $5-140°$ in vertical direction and at $10-140°$ in horizontal direction, whereas a dipole magnet provides bending power for particles exiting at angles smaller than 5° in vertical direction and 10° in horizontal direction.

2 Requirements on the $\overline{\text{P}}$ANDA Internal Targets

COMMENT: Author: A. Khoukaz, H. Orth, M. Büscher, V. Varenzo

2.1 Requirements

The experimental requirements for the internal target for $\overline{\text{P}}$ANDA are manifold and change with the different aspects to be investigated in the proposed measurements. In detail the following aspects have to be considered in the choice of the applied target type:

Target material
For most of the production and reaction studies, measurements in fundamental interactions, i.e. the scattering of anti-protons and protons, are required. Therefore, the main target material will be hydrogen and deuterium, where in the latter case the deuterons act as an effective neutron target. However, since also measurements on heavier nuclei are foreseen, the use of other materials such as N_2, O_2, He, Ne, Ar ,Xe etc. will be desirable.

Purity of the target material
The investigation of challenging reactions like e.g. the production of exotic particles in fundamental nucleon-anti-nucleon interactions implies that a highest purity of the applied target material has to be apparent. Any pollution of the target with other materials would result in disturbing background reactions which have to be understood in the later data analysis. To avoid inaccuracies caused by such background it is highly desirable to provide targets with both highest purity. Since proton and deuteron targets are of high interest for $\overline{\text{P}}$ANDA, the optimum target would provide pure hydrogen/deuterium in a gaseous, liquid or solid phase. Fiber targets such as CH_2 would not be acceptable since they contain additional elements (carbon). Furthermore, liquid hydrogen/deuterium in vacuum chambers is commonly provided in target cells, which have the disadvantage of window material causing background reactions. Additionally, they have usually a too high areal density in order to be acceptable as target for internal beam experiments at storage rings. Therefore, beams of gaseous or solid state hydrogen/deuterium will be best suited for such experiments.

Vacuum conditions
At PANDA anti-protons with only a limited production rate will be stored and accelerated. Due to this, residual gas background in the $\overline{\text{P}}$ANDA vacuum system has to be reduced as good as possible in order to avoid anti-proton losses outside the interaction region. Additionally, such residual gas background would cause disturbing background in the recorded data. Due to this restriction a use of a conventional (supersonic) gas-jet beam is excluded since here a large broadening of the target beam even shortly after its production is observed. Thus, the most convenient types of target for $\overline{\text{P}}$ANDA are given by beams of **cluster-jets** and **pellets**. Both fulfill the previously mentioned requirements.

Areal target density
Since $\overline{\text{P}}$ANDA is designed as an fixed target experiment at the internal anti-proton beam, the areal target density has to be significantly below $\rho = 10^{16}$ nucleons/cm^2 in order to avoid large beam heating effects which will not be compensable by the foreseen anti-proton beam cooling systems. Furthermore, the target must be thin enough to avoid multi-scattering and interactions of the ejectiles in the target material. On the other hand depending on the reaction type to be investigated the target has to provide sufficient density in order to allow for the design luminosity of $L_{max} = 2 \cdot 10^{32}$ cm$^{-2}s^{-1}$. This design luminosity is limited by the anti-proton production rate $\dot{N}_{\bar{p}}^{+} \leq 2 \cdot 10^7$ $\bar{p}$/s which corresponds to the upper limit of the average anti-proton consumption in experiment:

$$\overline{\dot{N}_{\bar{p}}^{+}} \geq \overline{\dot{N}_{\bar{p}}^{-}}. \tag{2.1}$$

The anti-proton consumption itself is given by the luminosity L and total cross section σ_{tot}. At an HESR beam momentum of $p = 1.5$ GeV/c the total cross section for interaction with a proton target amounts to $\sigma_{tot} \approx 100$ mb. Therefore, the maximum mean luminosity is given by

$$L_{max} = \overline{\dot{N}_{\bar{p}}^{+}} \cdot \sigma_{tot} \approx 2 \cdot 10^{32} cm^{-2} s{-}1. \tag{2.2}$$

This in turn sets an upper limit on the reasonable areal target density in experiment:

$$\rho_{target,max} = \frac{L_{max}}{N_{beam} \cdot f_{beam}}, \tag{2.3}$$

with N_{beam} as the number of stored particles in the ring and f_{beam} as the revolution frequency of the anti-protons. With $N_{beam} = 10^{11}$ anti-protons and

$f_{beam} = 443$ kHz, the maximum useful target beam density is equivalent to

$$\rho_{target,max} = 4.5 \cdot 10^{15} atoms/cm^2. \quad (2.4)$$

Adjustable target density
Depending on the experimental conditions an adjustment of the luminosity below the maximum possible will be necessary. This might be achieved by two methods:

- Reduction of the anti-proton intensity.
- Reduction of the target beam density.

Although both solutions will lead to a reduction of the luminosity, the latter method, i.e. the adjustment of the target beam density to an optimum vale, is the preferable way. This is due to the fact that a reduced target density coincides with reduced beam heating and smearing effects. In addition, this solution allows for a reduced probability of secondary interactions of the reaction products in the targets as well as less gas load to the scattering chamber which in turn minimizes interactions on residual gas. Furthermore, due to the consumption of anti-protons during an accelerator cycle a corresponding increase of the target density will be advantageous in order to obtain constant event rates and thus a constant luminosity during a cycle.

Homogeneous volume target density
The use of a cooled anti-proton beam at PANDA will lead to an accelerator beam diameter of $\varnothing_{beam} \leq 100$ μm. Therefore, the target beam at the interaction region should be as homogeneous as possible. A significant granularity such as it is apparent in case of a pellet beam in combination with an angular spread of the target particles will require for an extended accelerator beam in the order of the mean distance between the individual target particles.

Absence of time structures
Under ideal conditions a target exposes no time structures on a microscopic time scale, which corresponds to the equivalence of both the mean luminosity $\bar{L}$ and the peak luminosity L_{peak}. However, any significant granularity of the target beam will lead to a larger factor for the ratio $L_{peak}/\bar{L}$ which in turn might cause unacceptable dead times or inefficiencies of both the data acquisition system and the detector components. Therefore, in order to guarantee a constant luminosity even on a microscopic time scale the absence of a time structure of the target beam is necessary.

Pointlike interaction zone
The investigation of short-living particles and their decay particles might require the reconstruction of the interaction vertex point with a precision much below 1 mm. For this purpose the knowledge of the beam-target interaction region with even a better resolution will be required. However, this request can only be fulfilled if a target with a high granularity is used (see previous topic) in combination with an additional tracking system to reconstruct the position of the target particle at the time of the interaction.

It is obvious that a single target system cannot fulfill all those wishes simultaneously. However, both a cluster-jet target as well as a pellet target meet a large fraction of the listed requirements and mutually complement each other. Therefore, to exploit the capacities of the $\overline{\text{P}}$ANDA experiment to a maximum it is foreseen to provide both a cluster-jet as well as a pellet source which will be installed alternatively depending on the experimental program to be investigated. A comparison of the different advantages and disadvantages of both a cluster-jet target and a pellet target is presented in table 2.1. Details on the properties of both types of targets will be given in the corresponding chapters.

Table 2.1: Comparison of the advantages of a cluster-jet target and a pellet target.

	cluster	pellet
target material	$\oplus\oplus$	$\oplus\oplus$
areal target density	$\oplus$	$\oplus\oplus$
adjustable target density	$\oplus\oplus$	$\ominus$
homogeneous target density	$\oplus$	$\ominus\ominus$
absence of time structures	$\oplus$	$\ominus\ominus$
pointlike interaction zone	$\ominus\ominus$	$\oplus$

2.2 Additional Types of Targets for $\overline{\text{P}}$ANDA

3 Organisation and Management

COMMENT: Author: A. Khoukaz

The two main internal targets for $\overline{\text{P}}$ANDA, the cluster-jet target and the pellet target, are build by eight groups from universities and research institutes in Germany, Italy, Russia, and Austria.

3.1 Work Packages and Responsibilities

Seven distinct main work packages have been identified. These comprise the design and construction of the following items.

1. The cluster-jet source. The overall responsibility is taken by WWU, Münster.
2. The pellet source. The overall responsibility is taken by FZJ+JCHP, Jülich.
3. The pellet tracking system. The overall responsibility is taken by IKP+TSL, Uppsala.
4. The target beam dump. The overall responsibility is taken by INFN, Genova.
5. The vacuum pipe system inside the solenoidal magnet. The overall responsibility is taken by FZJ+JCHP, Jülich.
6. The gas supply system. The overall responsibility is taken by SMI, Austria.
7. The slow control system. The overall responsibility is taken by NN, NN.

Additionally, the following related working packages have been identified:

1. The mechanical interface. The overall responsibility is taken by FAIR+GSI, Darmstadt.
2. The safety system. The overall responsibility is taken by FAIR, Darmstadt.

A detailed list of work packages has been worked out, and responsibilities have been identified, which have been approved by all groups.

Task	Responsible
Cluster Jet Source	
Design, construction	WWU, GSI
Assembly and tests	WWU
Transport to FAIR	WWU
Assembly at FAIR	WWU, GSI
Commissioning at FAIR	WWU, GSI
Pellet Source	
Design, construction	FZJ, ITEP, MPEI
Nozzle production	FZJ, ITEP
Assembly and tests	FZJ, ITEP, MPEI
Transport to FAIR	FZJ
Assembly at FAIR	FZJ
Commissioning at FAIR	FZJ, ITEP, MPEI
Pellet Tracking System	
Design, construction	UU, FZJ
Assembly and tests	UU, FZJ
Prototype operation at WASA-at-COSY	UU, FZJ
Assembly at FAIR	UU, FZJ
Commissioning at FAIR	UU, FZJ
Target Beam Dump	
Design, construction	INFN, GSI, WWU, FZJ
Assembly and tests	INFN, GSI
Transport to FAIR	GSI
Assembly at FAIR	GSI
Vacuum Pipe System	
Design, construction	FZJ, WWU, GSI
Assembly and tests	FZJ, GSI
Transport to FAIR	FZJ
Assembly at FAIR	FZJ
Gas Supply System	
Design, construction	SMI, WWU, GSI, FZJ
Assembly and tests	SMI
Transport to FAIR	SMI
Assembly at FAIR	SMI
Slow Control System	
Design, construction	SMI, INFN, GSI
Programming	SMI, INFN, GSI
Assembly and tests	SMI, INFN, GSI
Transport to FAIR	SMI, INFN, GSI
Commissioning at FAIR	SMI, INFN, GSI

Table 3.1: List of work packages.

¡¡¡¡¡¡¡ .mine

4 Cluster Jet Target

COMMENT: Author: A. Khoukaz, H. Orth

4.1 Production of Cluster Beams

Cluster-jet beams for internal storage ring experiments at are commonly produced by expansion of pre-cooled gases in fine Laval-type nozzles into vacuum. During the passage of the gas through such a nozzle the gas cooles down according to adiabatic cooling supported by the Joule-Thomson effect of real gases and can form a supersonic beam. Under appropriate conditions, depending on the type of gas, condensation can take place and nano-particles can be created, the so-called *clusters*. The size of such clusters is strongly influenced by the experimental conditions such as the pressure and the temperature of the gas before entering the nozzle. Furthermore, the diameter as well as the shape of the used nozzle influences both the size of these particles and the total cluster yield.

Due to the fact that the produced clusters are typically in the nanometer scale they reveal important features for the usage as target particles in storage ring experiments. One of the most important aspects is the fact that, due to the large mass compared to incoming molecular gas, nearly no angular smearing of the particle trajectories are observable caused by scattering with residual gas. Therefore, cluster jet beams can travel over several meters of distance in vacuum chambers without disturbance of the direction or shape. This is in clear contrast to (supersonic) gas jet beams which are strongly affected by residual gas and expose a strong spatial widening already after few centimeters, which in turn is associated with a corresponding decrease in beam density by orders of magnitude.

In Fig. 4.1 a drawing of a CERN-type nozzle is shown. This design was and still is used successfully in many devices for production of supersonic and cluster-jets beams [1, 2, 3, 4]. Depending on the experimental conditions and requirements, minimum opening diameters of 11-100 μm are commonly used. The formation of supersonic beams and the production of cluster-jets can be described in a pT-diagram, displaying the pressure of the expanding gas inside of the nozzle as function of the temperature. In Fig. 4.2 such a situation is shown qualitatively for starting parameters p_0 and T_0 as

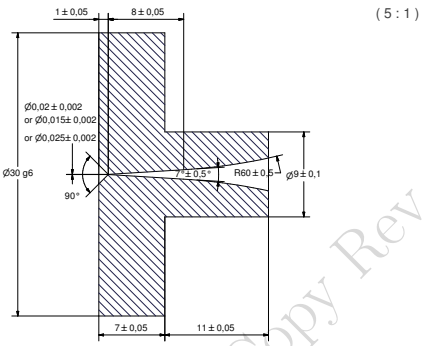

Figure 4.1: Sketch of the used Laval-type nozzles produced at CERN.

the pressure and temperature of the gas before entering the nozzle. During the expansion, which can

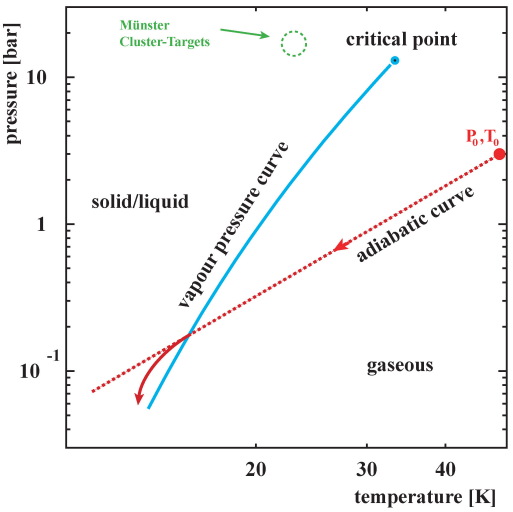

Figure 4.2: Vapour pressure curve for hydrogen gas as function of the gas temperature and of the gas pressure. The dotted curve represents the adiabatic expansion of a gas with an initial temperature T_0 and pressure P_0. The preferred region of operation of cluster-jet targets of the Münster type is indicated.

be described in good approximation by an adiabatic process, both the pressure and the temperature of the gas decrease drastically. Depending on the geometry of the nozzle and the starting parameters p_0 and T_0 the adiabatic curve can cross the

vapour pressure curve. In this regime the previously gaseous target material enters the fluid phase and condensation can take place, which in turn causes an additional pressure decrease. In case of hydrogen as target material typical starting parameters of conventional cluster-jet target sources are temperatures in the order of T = 25-35 K and pressures of p $\leq$ 10 bar, which means that the used hydrogen is still in a gaseous phase before entering the nozzle. Being dependent of the experimental conditions the size of clusters amounts to typically 10^3-10^5 atoms per particle. Thus a cluster-jet beam corresponds to good approximation to a target beam with homogeneous volume density. A speciality of the Münster-type cluster-jet targets, which are routinely used in storage ring experiments [1, 4], is the operation in a regime where the gas is already in the fluid phase before entering the nozzle (see Fig. 4.2). By this much higher target densities are accessible compared to conventional cluster-jet sources. This in turn enables for the production of cluster-jet beams which meet the requirements at $\overline{\text{P}}$ANDA. Due to this highly increased cluster-jet density it is possible to directly observe the target beams behind the production nozzle. In Fig. 4.3 a photography of such an intense cluster-jet beam is shown. The beam, illuminated by an LED in the vacuum system, leaves the nozzle (not visible) and moves from the left to the right. Also not visible are the collimators which are placed behind the nozzle and determine the shape and size of cluster-jet beam at the later interaction point.

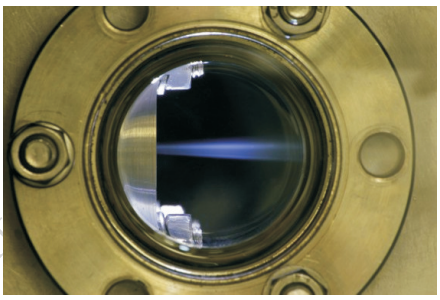

Figure 4.3: Image of a hydrogen cluster-jet beam directly after passing the nozzle. The cluster-jet is illuminated by a photo-diode array in the vacuum chamber.

The high-intense cluster-jet source for $\overline{\text{P}}$ANDA will typically be operated in the fluid phase before entering the nozzle to obtain highest target beam densities. However, similar to conventional cluster-sources the $\overline{\text{P}}$ANDA cluster-jet generator can be operated in a wide range of gas temperatures and gas pressures. Due to this the areal target beam density at the later interaction point can be adjusted according to the experimental requirements. This situation is demonstrated in Fig. 4.4, presenting the hydrogen atom flow F at the scattering chamber as function of the nozzle temperature and the gas input pressure. In the gaseous regime of operation before entering the nozzle comparatively low densities are achieved. However, when passing the vapour pressure curve, indicated by the white line in Fig. 4.4, highest particles flows are observed, which is equivalent to highest target beam densities. The

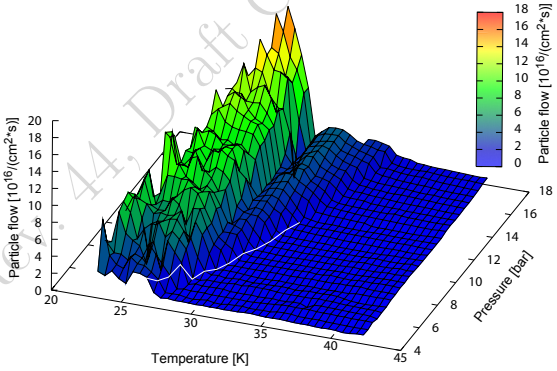

Figure 4.4: Hydrogen atom flow through the scattering chamber as function of the nozzle temperature and the gas input pressure.

presented hydrogen atom flow F in the scattering chamber can directly be translated into an areal target density

$$\rho_V = \frac{F}{v}, \tag{4.1}$$

with v as the velocity of the cluster-jet beam. Therefore, with the knowledge of the cluster velocities the particle flow can directly be transformed into an volume density of the cluster-jet beam at the scattering chamber. Details on the determination of the velocities will be given in section 4.2.

Since cluster-jet beams are produced by expansion of pressurized and pre-cooled gas through fine nozzles, highest purity of the used gas is of utmost importance. The presence of any micro-particles would lead to an irreversible blocking of the nozzle. Furthermore, since for the operation at $\overline{\text{P}}$ANDA hydrogen and deuterium gas are of highest relevance to provide effective proton and deuteron targets, any contamination with other gases like oxygen, nitrogen etc. would lead to reversible blocking of the

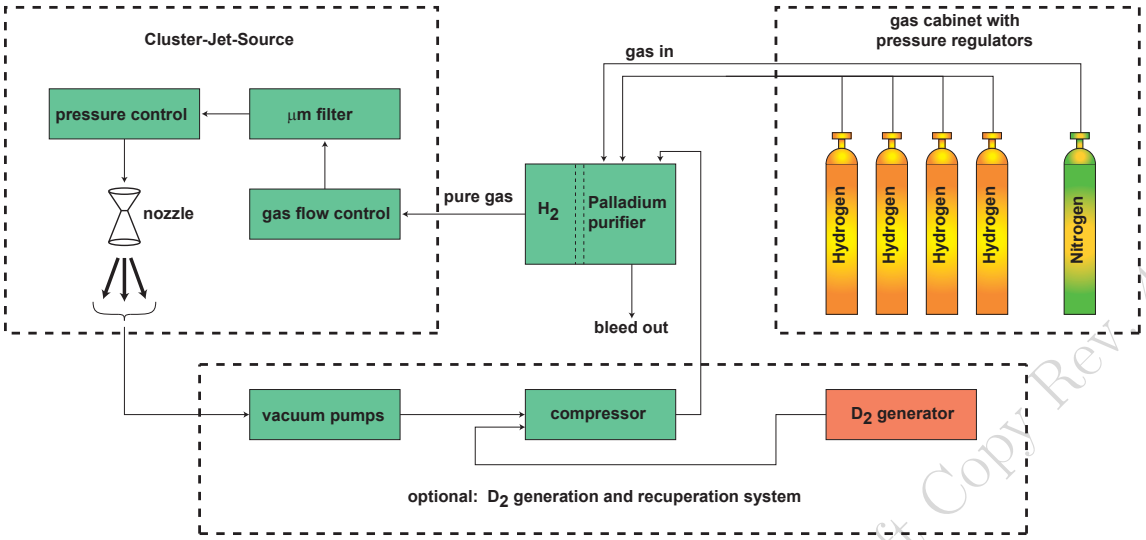

Figure 4.5: Schematic drawing of a gas supply system for the cluster-jet source.

cooled nozzle ($T \leq 30K$) during operation. The latter kind of blocking can be remedied by heating of the nozzle system, however, since such a warm-up procedure corresponds to an effective luminosity reduction, the gas supply system must guarantee highest quality. In Fig. 4.5 a block diagram of a gas supply system is shown which is routinely used for the cluster-jet targets at COSY [5] and in Münster and which fulfils the described requirements. In this arrangement hydrogen/deuterium gas is fed to a purifier system based on a heated palladium membrane. By this gas of ultra-high purity can be provided leading to stable nozzle operations over weeks. In addition micro-filters are used in the gas lines close to the nozzle.

To prepare cluster-jet beam conditions according to the experimental requirements, gas flow and pressure controls are used in addition to a temperature control system. After expansion of the gas in the nozzle the used gas is finally removed by vacuum pumps. In case of operation with comparatively expensive deuterium a recuperation system is used which cleans the pumped gas and feed it into a gas compressor. Here the gas is pressurized again to the nominal value and fed to the palladium purifier. The deuterium gas itself can either be provided conventionally by gas bottles or by a D_2-generator. The latter device, operated with heavy water, converts D_2O electrolytically into D_2 gas, which in turn is lead to the compressor unit. Details on the gas supply system for PANDA are given in section 9.

4.2 Cluster Beam Properties

The precise knowledge of the properties of cluster-jet beams as well as of the individual clusters itself is an important input for both the development and optimization of cluster-jet sources and the later operation in storage ring experiments. Especially information on the size and velocity distributions of the clusters are of high interest since they are directly correlated with the absolute density of the cluster-jet beam at the interaction point as well as with its homogeneity.

The mass flow G_m through a Laval-type nozzle is dependent on the properties of the nozzle and the used gas and can be written as

$$G_m = A^* \cdot p_0 \cdot \sqrt{\frac{M_{mol} \cdot \kappa}{R \cdot T_0}} \cdot \left(\frac{2}{\kappa + 1}\right)^{\frac{\kappa+1}{2(\kappa-1)}}, \quad (4.2)$$

with the minimum cross-sectional area inside the nozzle A^*, the pressure, temperature and molar mass of the incoming gas p_0, T_0 andM_{mol}, as well as the adiabatic exponent $\kappa = c_p/c_v$. Assuming an ideal gas expanded into vacuum by using a Laval-type nozzle, the incoming gas is converted into an almost monoenergetic gas beam with a maximum velocity of

$$v_{max} = \sqrt{\frac{2\kappa}{\kappa - 1} \cdot \frac{R \cdot T_0}{M_{mol}}}. \quad (4.3)$$

By feeding the nozzle with hydrogen in a gaseous phase, the clusters are produced and embedded in-

side the nozzle in a gas beam. Therefore, the velocity of the produced clusters can be described in first approximation by the velocity of the conventional gas beam which surrounds the cluster-jet.

In Fig. 4.6 a calculation for the gas beam velocity during the passage through a Laval-type nozzle is shown as function of the distance from the minimum opening inside the nozzle. As can be seen the gas is strongly accelerated shortly after the minimum diameter and reaches its maximum velocity already a after few millimeters. This increase of

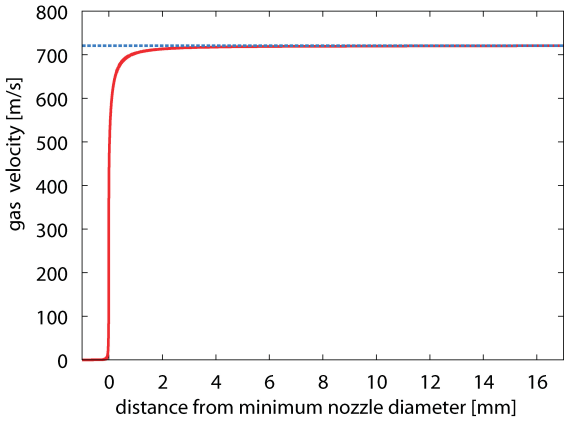

Figure 4.6: Calculation of the gas beam velocity during the passage through a Laval-type nozzle with a diameter of d = 28 μm. The temperature of the gas before entering the nozzle amounts to 25 K. The smallest diameter of the nozzle is located 1 mm after the nozzle entrance.

the velocity is directly connected with a strong decrease of the gas pressure as well as of the temperature of the gas beam. The maximum velocity, given by eqn. 4.3, depends for an ideal gas only on the input temperature of the gas. However, since hydrogen and deuterium are real gases it is expected that the gas velocities and thus the cluster velocities differ from this simple approximation. In order to measure the velocities of individual clusters and to compare them with calculations, a time-of-flight device has been built-up at the University of Münster which allows to ionize single clusters by an pulsed electron beam and to detect them using a channeltron [6]. In Fig. 4.7 a measurement is shown for a cluster beam produced at a nozzle temperature of T = 50 K. As can be seen the the cluster beam exposes a finite velocity distribution, reflecting the cluster production processes as well as the particle interactions inside the nozzle. Additionally, the mean velocity is slightly below the value calculated by eqn. 4.3 and indicated by the dashed line.

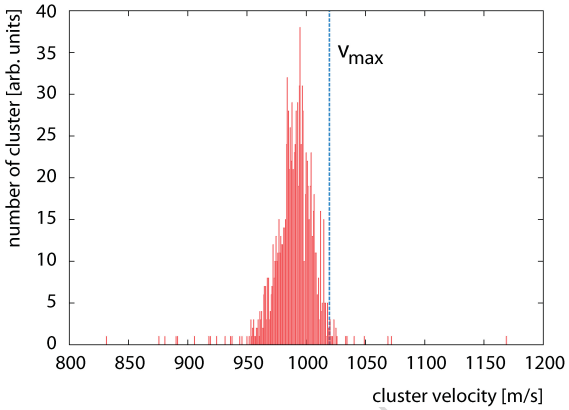

Figure 4.7: Cluster beam velocity distribution obtained at a nozzle temperature of 25 K and a gas input pressure of 8 bar. The maximum possible velocity is indicated by the dashed line.

Although the deviation from v_{max} as well as the observed velocity width are here obviously of minor relevance, this situation might change when the target source is operated in the fluid phase before entering the nozzle. Therefore, detailed studies on the velocities and velocity distribution of hydrogen cluster beams have been performed [6]. In Fig. 4.8 the measured cluster-jet velocities are displayed as function of the nozzle temperature which directly corresponds to the temperature T_0 of the incoming hydrogen. While above T = 30 K the measured ve-

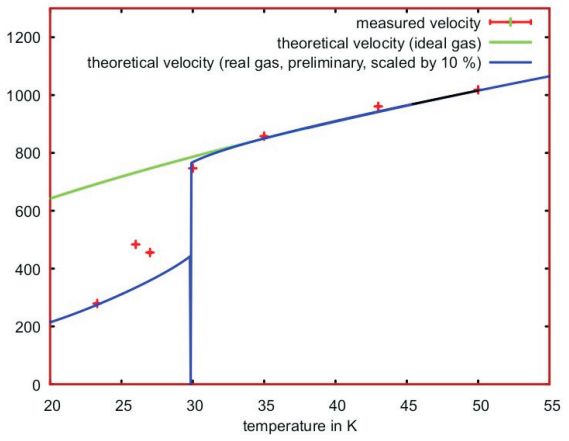

Figure 4.8: Cluster velocities (in units of m/s) as function of the nozzle temperature, obtained at a gas input pressure of p = 8 bar. In the gaseous regime (T > 30 K) the cluster velocity can be described well by model calculation assuming an ideal gas. At lower temperatures the properties of a real gas/fluid have to be taken into account to describe the measured velocities.

locities can be described well by eqn. 4.3 for an ideal gas, the situation changes significantly at lower temperatures where the incoming hydrogen is already in a fluid and/or supersaturated phase. More detailed calculations [7] considering the properties of a real gas/fluid expose that the velocity is also dependent on the gas input pressure and succeed to describe the measured distributions. The agreement between these calculations and the experimental results proof that the cluster velocities agree in good approximation with the gas beam velocities.

An further important property of a cluster-jet beam are the shape and the homogeneity of the beam at the region of interaction with the storage ring beam. While conventional (supersonic) gas-jet expose a gaussian spatial density profile in combination with a rapid density decrease with propagation direction, cluster-jets show (a) a homogeneous volume density distribution, (b) a sharp boundary, and (c) a constant angular divergence determined by the collimators used at the cluster-jet source. This situation is presented in Fig. 4.9 displaying the areal density profiles of a cluster-jet beam in both directions transverse to the spread direction of the target beam, measured 2.1 m behind the nozzle. The observed areal density distributions are in good agreement with the expectations assuming a cylindrical beam with constant volume denity. Therefore, even after several meters of passage through a vacuum system the cluster-jet beam preserves its properties which makes it perfectly suited as a target beam for storage ring experiments.

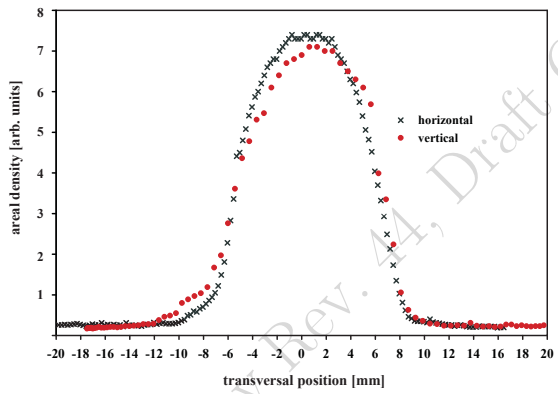

Figure 4.9: Density profiles of a hydrogen clster-jet beam recorded with a monitor system located at the virtual PANDA interaction zone. The cluster-beam has been scanned in both directions transverse to the spread direction of the target beam. Due to the finite width of the scanning rods the sharp boundary of the cluster-jet beam appears as a smeared distribution.

4.3 Cluster Beam Densities

Among many other parameters the absolute areal density of a target beam at the interaction point is an important quantity in a storage ring experiment. Here several aspects have to be taken into account:

- Target beam time structure
- Compatibility of the peak/mean event rate with the data acquisition system as well as with the detector components
- Accelerator beam heating and beam cooling power
- Lifetime of the accelerator beam
- Adjustability of the target beam density during the experiment
- Required luminosity

One of the advantages of a cluster-jet target is the homogeneous volume density distribution which results in an absence of time structures in a storage ring experiment. This aspect is of high importance since any significant microscopic time structure in the target density would lead to a corresponding effect in luminosity. Furthermore, the absolute areal target density can be adjusted easily during operation, which allows to operate the target at densities which are optimized to phase space cooling devices for the accelerator beam. Additionally, the possibility to adjust the target density within seconds/minutes allows to increase the density during the accelerator cycles in order to compensate beam anti-proton beam losses and to provide constant event rates. The possibility to vary the target density is demonstrated in Fig. 4.10 showing the areal target beam density at the interaction point in the scattering chamber as function of the nozzle temperature. Obviously the absolute target density and thus the luminosity can be adjusted continuously over several orders of magnitude. A similar effect can be achieved by changing the gas input pressure. It is important to note that these density variations can be performed during target operation.

The currently available absolute target density in combination with PANDA-geometry is presented in Tab. 4.1 ("Münster") and compared to cluster-jet target facilities operated at CELSIUS, FERMILAB and COSY. The main challenge of a cluster-jet target for the PANDA experiment is the comparatively large distance between the nozzle and the interaction point of d = 2.1 m which is a factor of 3-8

Table 4.1: Comparison of operation parameters and obtained target densities of different cluster-jet targets. Note that the densities observed in Münster are obtained at a distance of more than two meters behind the nozzle, i.e. in PANDA geometry.

	CELSIUS	E835 FERMILAB/GSI	ANKE and COSY-11	Münster
nozzle diameter	100 mm	37 mm	11-16mm	11-28 mm
gas temperature	20-35 K	20-32 K	22-35 K	20-35 K
gas pressure	1,4 bar	<10 bar	18 bar	> 18 bar
distance from nozzle	0,32 m	0,26 m	0,65 m	**2,1 m**
target density	$1.3{\cdot}10^{14}$ cm^{-2}	$> {\cdot}10^{15}$ cm^{-2}	$\gg 1 \cdot 10^{14}$ cm^{-2}	$\mathbf{8{\cdot}10^{14}}$ **cm**$^{-2}$

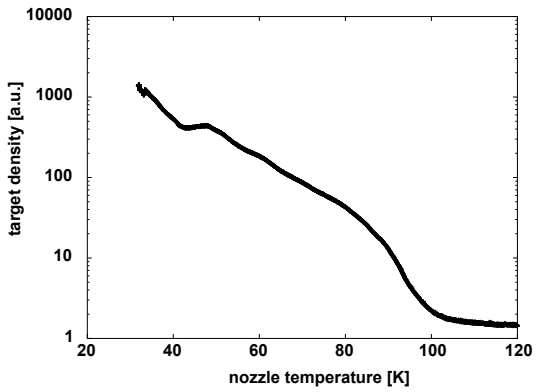

Figure 4.10: Areal density of the cluster-jet beam at the interaction point in the scattering chamber as function of the nozzle temperature. The absolute target density and thus the luminosity can be adjusted continuously over several orders of magnitude.

larger than in previous experiments. Since the volume density ρ_{volume} scales with the distance l according to

$$\rho_{volume} \sim \frac{1}{l^2}, \tag{4.4}$$

this increase of distance requires an increase of the effectiveness of the target source by at least one order of magnitude to provide same target densities at that distance. Systematic studies on the improvement of the cluster yield showed that such high cluster yields can be obtained by special operation of the cluster source [4, 6, 7] and areal target densities of $\rho_{areal} = 8 \cdot 10^{14}$ atoms/cm^2 have been reached. Current improvements on the prototype for the cluster source for PANDA are expected to lead to even higher numbers.

4.4 Cluster Beams of Heavier Gases

During recent systematic investigations on the optimization of cluster-jet sources for storage ring experiments [6, 7, 8, 9] the main focus was set on the production of hydrogen cluster beams. These studies on this single type of gas is motivated by the high interest of most experimental programs to investigate reactions and production processes in elementar interactions on nucleons, i.e. protons [10]. Since the chemical and physical properties of hydrogen and deuterium are quite similar, the recently prepared cluster-sources are at same time highly suitable to produce and prepare deuteron cluster-jets, which in turn might serve as effective neutron targets. The capability with respect to deuterium cluster-jets has already been shown in storage ring experiments [11] and such beams are routinely used i.e. in high-luminosity meson production experiments [11, 12].

Since studies on heavier nuclear targets are also under discussion at PANDA an operation of the PANDA cluster-jet source with heavier gases as cluster material is foreseen. Due to the much higher condensation temperature, in practice the production of such heavy gas clusters turn out to be even easier to realize than the formation of hydrogen/deuteron clusters. Clusters of CO_2 for example can be produced without cooling already at room temperature. Already in the past cluster-jets of heavy gases such as Xenon have been produced and used in storage ring experiments [2, 13]. In order to allow the operation of the PANDA cluster source with heavier gases the integrated cooling and heating devices will be adjusted to operate the cluster-jet targets with gases like H_2, D_2, O_2, N_2, Ne, Ar, Xe.

4.5 Cluster Beam Source for PANDA

Based on the recent intensive studies on the development and optimization of high-intense cluster-jet sources for storage ring experiments [6, 8] a prototype for the PANDA cluster-jet source was build-up and set into operation at the University Münster. A cross section of this cluster source is given by the CAD-drawing shown in Fig. 4.11[1]. The CERN-type nozzle with diameters between 11 μm and 40 μm is mounted on top of a copper holder, which itself is connected to a two-stage cryogenic coldhead (type MD10, Oerlicon-Leybold) of high cooling power in combination with only moderate vibrations. As has been shown by previous cluster-jet target installations, the use of such coldhead systems using closed helium circuits are highly suited for such purposes since they combine high cooling power, large maintenance intervals and simple operation. Different to conventional coldheads the chosen type allows for an adjustment of the compressor power which can be changed according to the experimental requirements.

In order to combine high thermal conductivity as well as gas tightness, the nozzle is sealed with a thin indium foil to the copper holder. The used gas is led through thin copper pipes which are cooled down by both stages of the coldhead and is fed to the nozzle. Due to the high cooling power of the applied coldhead this arrangement is capable to cool down the nozzle as well as the gas down below 20 K in operation.

Two heating cartridges are integrated in the copper nozzle holder with a total heating power of P_{heat} = 50 W. Operated by an external control unit this heating device is capable to stabilisize the temperature of the nozzle/gas with a precision of less than 0.1 K. Additionally, the gas input pressure is adjusted by an external control unit which allows for stable pressure conditions. By this it is possible to guarantee stable target thicknesses during the experiments.

To avoid heat transfer between the two coldhead stages as well as from the warm stage to the outer flanges the corresponding pipes are made by stainless steel which has a much lower heat conductivity as copper. Furthermore, for same reasons the complete gas pipe arrangement as well as the cold stages of the cryogenic system are placed inside an insulation vacuum stage which is evacuated by a turbomolecular pump. This insulation vacuum chamber is separated from the next vacuum stage, the so-called skimmer chamber, by a membrane bellow arrangement.

In the skimmer chamber the outlet of the nozzle is located which means that here most of the gas flow into the vacuum system is present. To enable vacuum pressures of $p_{skimmer} \leq 10^{-1}$ mbar at maximum at this stage, two rotary vane pumps located close to the cluster source will be used at PANDA. The produced cluster-jet beam, surrounded by a conventional supersonic gas-jet, is shot onto a skimmer to subtract the gas beam from the clusters. For the final cluster-jet beam preparation a second skimmer, the collimator, is used in the following collimator vacuum stage. The collimator stage itself is pumped by two turbomolecular pumps.

Both skimmers with diameters below d = 1 mm separate the neighbouring differential vacuum chambers from each other and allow for an effective reduction of the residual gas background. From here on the cluster-jet beam passes the complete target beam pipes with a constant opening angle, defined by the geometry of the nozzle/skimmer/collimator arrangement.

In order to switch the target beam on or off within seconds during experimental runs at PANDA, a nozzle shutter (not visible) will be installed in the skimmer chamber between the nozzle outlet and the first skimmer. Additionally, a camera system will be fixed to a window at one of the vacuum flanges in order to monitor the cluster-jet beam in the skimmer chamber during operation.

In Fig. 4.12 a photography of the completely mounted inner part of the prototype for the PANDA cluster source is shown. Clearly visible are the copper and stainless steel gas pipes arranged around the cryogenic coldhead. The cables are used both for temperature readout as well as for the power supply of the heat cartridges. The two thick pipes at the lower left side of the coldhead are the connectors for the helium compressor unit.

Since both the shape as well as the diameter of the cluster-jet beam at the later interaction point at PANDA will be determined by the properties of the used skimmers, special care has to be taken with respect to their mechanical properties and their arrangement relative to the nozzle. To avoid turbulences at the point where the cluster/gas beam hits the skimmer it is advantageous to use a skimmer shape which guides the peeled off gas beam. In addition the wall material at the skimmer tip has to

1. Note that in the final installation at PANDA the cluster source is mounted upside down with respect to the presented orientation.

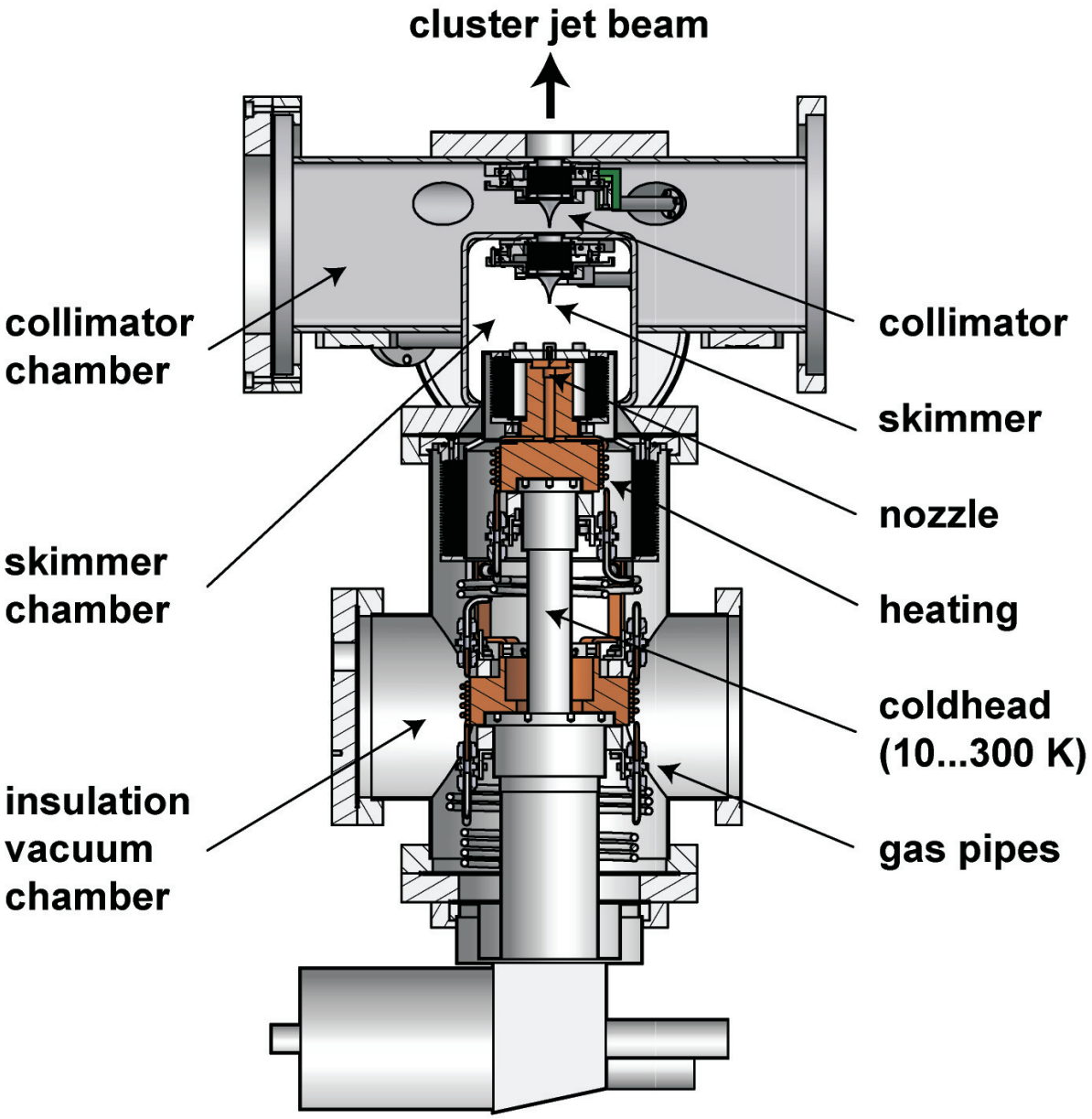

Figure 4.11: Sketch of the cluster-jet source for the $\overline{\mathrm{P}}$ANDA experiment. The (warm) gas can be cooled down to $T \sim 10$ K by a two-stage cryogenic coldhead and passes a Laval-type nozzle. The resulting cluster-jet beam, surrounded by a conventional supersonic gas-jet, is shot onto a skimmer to subtract the gas beam. For the final cluster-jet beam preparation a second skimmer, the collimator, is used in the collimator vacuum stage. From here on the cluster-jet beam passes the complete target beam pipes with a constant opening angle, defined by the geometry of the nozzle/skimmer/collimator arrangement. To avoid losses of cooling power due to unsufficient vacuum conditions the complete coldhead device including the gas pipes are located in a vacuum chamber separated from the nozzle chamber. Close to the nozzle an electric heating is mounted to allow for a temperature adjustment. Both the skimmer as well as the collimator are mounted on movable tables which can be moved with a micrometer precision. By this the position of the cluster-jet beam can be adjusted online during operation.

be as thin and sharp cut as possible to minimize effects of disturbing reflections. In practice special skimmers made by nickel are used directly after the nozzle which have at the very top a wall thickness

Figure 4.12: The complete mounted prototype of the PANDA cluster beam production head with the nozzle on the very top. Clearly visible are the gas pipes which are conneted to the coldhead. The cables are used for the electric connection of the nozzle heating system as well as for the silicon diodes used for the gas temperature measurement.

of only d = 10 μm. The opening diameter at this point can be varied according to the experimental conditions and is typically in the order of $\varnothing_{skimmer}$ = 700 μm.

In Fig. 4.13 a photography of the skimmer mounted on top of the skimmer holder is shown. This support part itself is placed on a moveable xy-table which allows to adjust the position of the skimmer in both direction perpendicular to the cluster-jet axis with on a micrometer scale. The adjustment is done via two step motor devices which are connected by special feedthroughs. In addition, an identical device is used for the collimator. Therefore, a variation of the skimmer position and thus of the cluster-jet beam during target operation is possible. Such adjustments are typically required for fine alignment directly after (re-)installation of the cluster source. Not visible here is an integrated membrane bellow which guarantees the vacuum tightness of this device.

Since the dimensions of the second skimmer (collimator) defines the shape and size of the cluster-jet

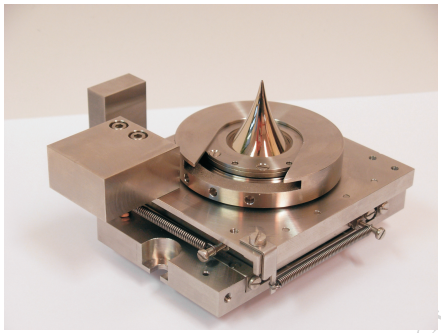

Figure 4.13: Skimmer with a minimum opening diameter of 700 μm mounted ontop of a table. With this device the skimmer can be adjusted in both direction perpendicular to the cluster-jet axis with on a micrometer scale. An identical device is used for the collimator.

beam at the interaction point special opening geometries can be chosen to meet experimental conditions. In Fig. 4.14 a CAD-drawing of a slit collimator is shown whose opening has been produced by a special laser cut process. In this special case a

Figure 4.14: CAD-drawing of a slit collimator produced by a special laser cut process.

slit opening of 70 μm × 700 μm has been manufactured for a special storage ring experiment [14] in order to provide a cluster-jet beam at the interaction zone with a horizontal width of of dx = 1 mm and a length in accelerator beam direction of dz = 10 mm. A microscopic view of this skimmer opening is presented in Fig. 4.15. At PANDA the use of such collimators with special geometry will be of high interest. Since the cluster-jet beam exposes a homogeneous volume density and the HESR anti-proton

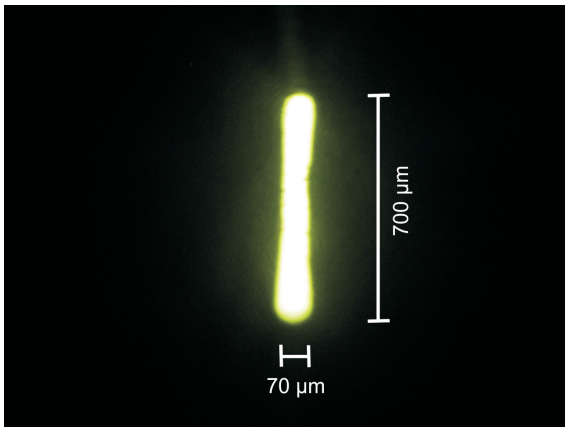

Figure 4.15: Microscopic view of the collimator produced by a laser cut process.

beam shrinks after acceleration and cooling to diameters below $\varnothing_{\bar{p}} = 100\ \mu$m, the extension of the cluster beam transversal to the HESR anti-proton can be in the order of $\varnothing_{jet} = 1$ mm or even below. Due to this the material transport through the $\overline{\text{P}}$ANDA scattering chamber into the target beam dump can be reduced by approximatively one order of magnitude. This in turn will lead to improved vacuum conditions in the interaction region.

4.6 Pumping and Vacuum System

In Fig. 4.16 a realization of the vacuum system for the cluster-jet target for the PANDA experiment is presented. The highest gas load ($\approx 4\,\mathrm{l}_n$/min) and pressure is present in the skimmer stage of the cluster source where the nozzle is located and the cluster-jet beam is produced. In order to guarantee pressures in the order of 10^{-1} mbar and below this stage is pumped in parallel by two identical pumping lines. Each of this lines consists of a high-power roots vacuum pump (RP) which itself is pumped by a second roots vacuum pump (RP) and, finally, by a forepump (VP).

To avoid losses with respect to cooling power, the main part of the surface of the cold head as well as the gas pipes are located in a separate vacuum stage, the insulation vacuum stage, which is pumped by a turbomolecular pump (TP). The skimmer vacuum stage is used here as forevacuum system. The cluster-jet beam passes the skimmer stage and enters the collimator stage which is connected by a conical aperture with a diameter of 700 μm. This vacuum chamber is pumped by two turbomolecular pumps (TP), which are evacuated by a separate pumping station, consisting of a roots vacuum pump (RP) and a forepump (VP). Finally, the cluster-jet passes the collimator stage which is separated again from the following stages by a conical aperture (700 μm).

Vacuum vales allow to separate different pumping units from the vacuum stages and allow for a simultaneous evacuation and venting of the complete vacuum source by one pumping line. This is important in order to avoid mechanical stress due to large pressure differences between neighboring vacuum chambers.

The interaction region of the $\overline{\text{P}}$ANDA experiment is separated from the cluster-jet source and the beam dump by two vacuum valves (V). Directly below the upper valve an additional differential pumped vacuum stage ist placed (intermediate stage), which allows for the reduction of the residual gas load to the $\overline{\text{P}}$ANDA scattering chamber. This stage is pumped by a turbomolecular pump (TP), which in turn is pumped by the forevacuum system of the collimator stage.

The lower part of Fig. 4.16 shows the realization of the target beam dump. Here it is foreseen to have a common solution which is designed for both the operation of the cluster-jet source as well as of the pellet source. The first part of the target beam dump will consist of three differential pumping stages, evacuated by two turbomolecular pumps (TP) each. The complete turbomolecular pump arrangement will be pumped by a roots vacuum pump (RP) and a final forepump (VP). The final beam dump stage will be evacuated by both a cryogenic pump (CP) as well as by a turbmolecular pump (TP). Depending on the used type of target source (cluster-jet or pellet), the inlay of this final vacuum chamber will be modified in order to guarantee optimum vacuum conditions. More details on the target beam dump as well as on the vacuum system will be given in sections 7 and 8.

4.7 Integration in $\overline{\text{P}}$ANDA

In Fig. 4.17 the integration of the $\overline{\text{P}}$ANDA cluster-jet source is illustrated. In the iron yoke of the superconducting solenoid magnet large openings (1000 mm × 1200 mm) have been foreseen in order to allow for the installation of the target source as close as possible to the interaction point. Placed above the magnet and close to the cluster-jet source the two pumping lines for the skimmer stage are foreseen, each consisting of two roots vacuum pumps and a forepump. The support frames for both the

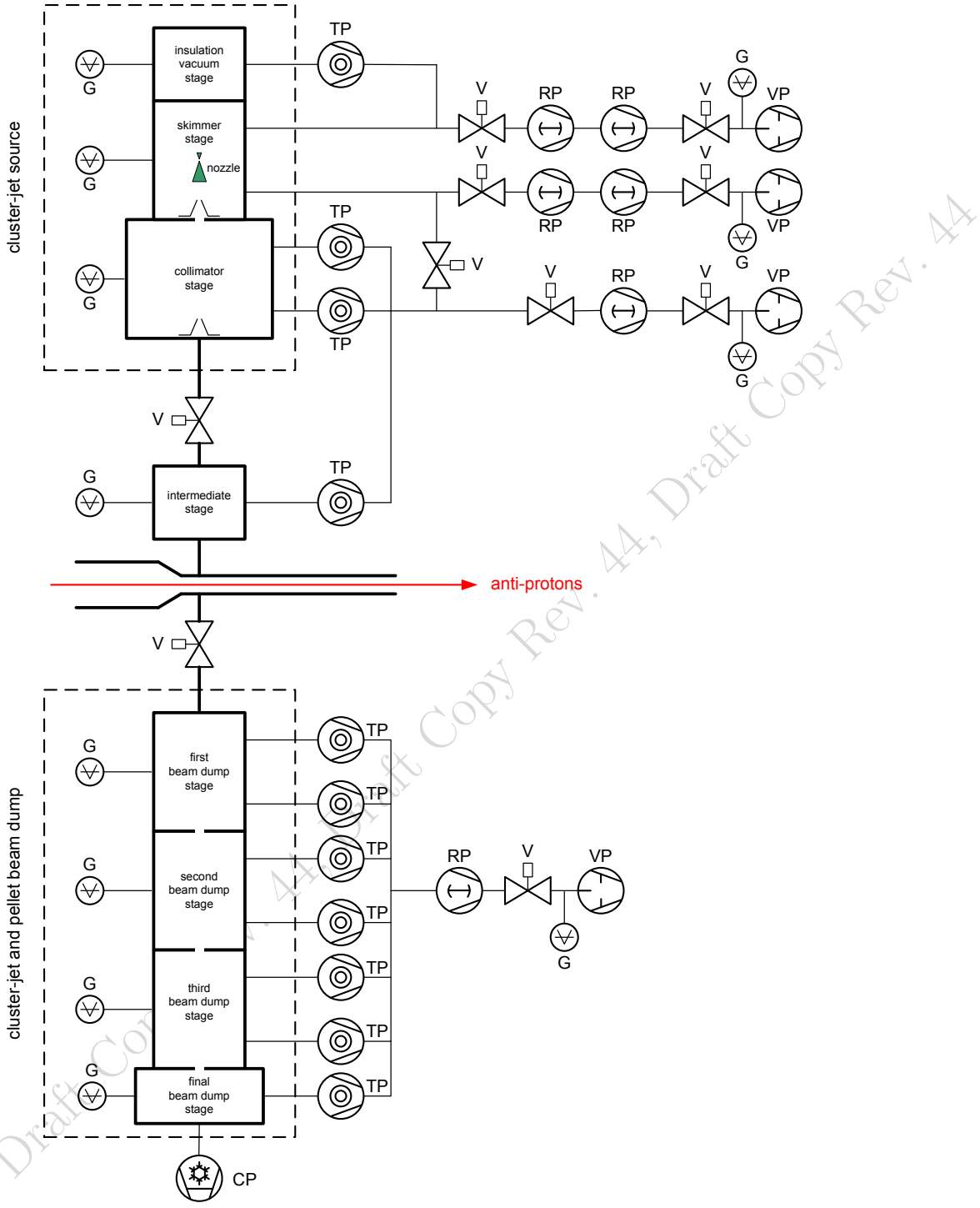

Figure 4.16: Schematic drawing of the vacuum system for the cluster-jet target.

target source as well as for the pumping stages (not shown in this figure) will be connected to the iron yoke in order to avoid mechanical excitations.

Cross sections of the cluster-jet target at the PANDA magnet are presented in Figs. 4.18 and Figs. 4.19. The openings in the magnet yoke al-

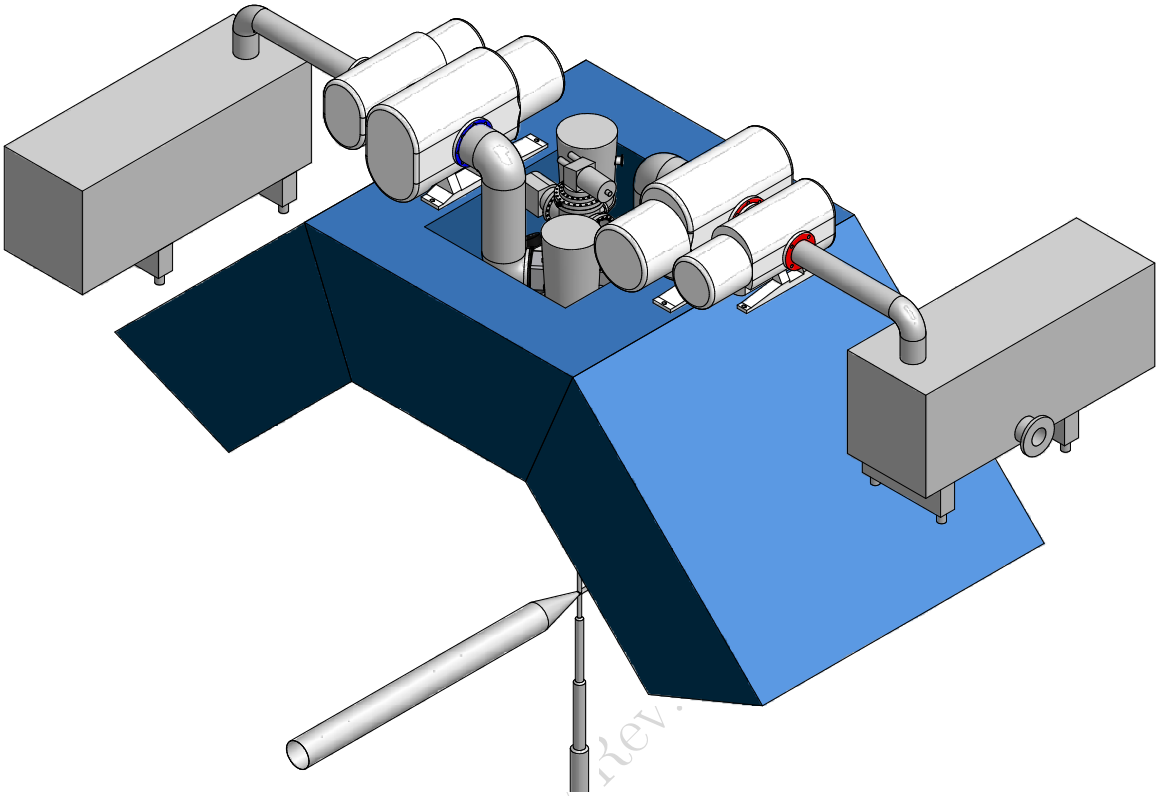

Figure 4.17: Schematic viewing of the integration of the cluster-jet source at $\overline{\text{P}}$ANDA. The support frames of both the target source as well as for the pumping stages (not shown in this figure) will be connected to the iron yoke in order to avoid mechanical excitations.

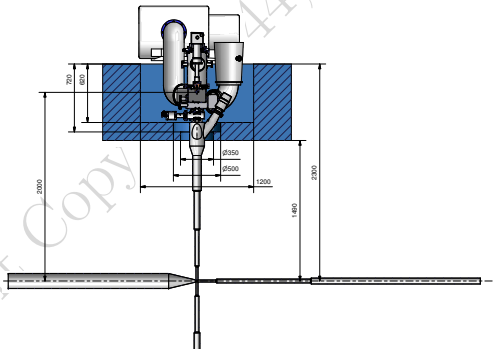

Figure 4.18: Cross section of the cluster-jet target at the $\overline{\text{P}}$ANDA magnet. The distance between the nozzle and the interaction zone amount to l = 2 m.

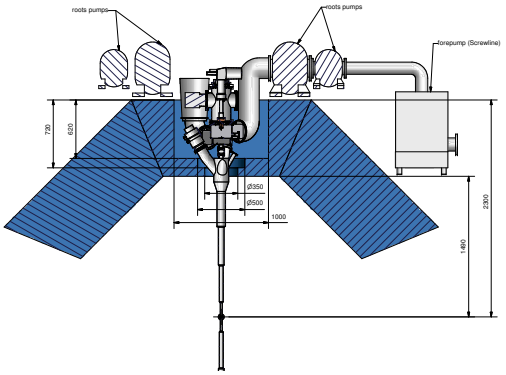

Figure 4.19: Cross section of the cluster-jet target at the $\overline{\text{P}}$ANDA magnet.

low for a distance between the nozzle and the interaction zone of l = 2 m. A top view of the installed cluster-jet source at $\overline{\text{P}}$ANDA is presented in Fig. 4.20.

Bibliography

[1] H. Dombrowski *et al.*, Nucl. Instr. Meth. **A 386** (1997) 228.

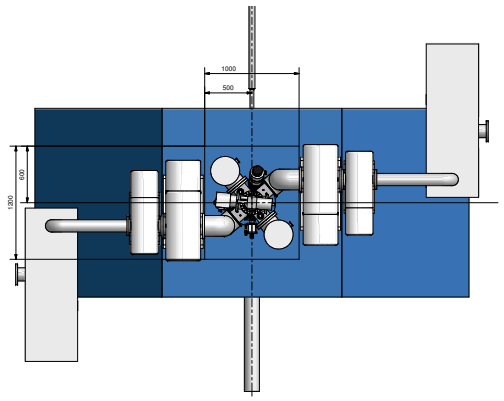

Figure 4.20: Top view of the installed cluster-jet source at PANDA.

[2] C. Ekström, Nucl. Phys. **A 626** (1997) 405.

[3] H.-H. Adam *et al.*, annual report 1998/99, Institut für Kernphysik, Westfälische Wilhelms-Universität Münster, p. 83

[4] A. Khoukaz *et al.*, Eur. Phys. J. **D 5** (1999) 275.

[5] H.-H. Adam *et al.*, annual report 1998/99, Institut für Kernphysik, Westfälische Wilhelms-Universität Münster, p. 85

[6] J. Otte, diploma thesis, Institut für Kernphysik, Westfälische Wilhelms-Universität Münster (2007).

[7] A. Täschner, doctoral thesis, Institut für Kernphysik, Westfälische Wilhelms-Universität Münster, in preparation.

[8] S. General, diploma thesis, Institut für Kernphysik, Westfälische Wilhelms-Universität Münster (2008).

[9] H. Orth, private communication (2008).

[10] PANDA Collaboration, Technical Progress Report, Technical report, FAIR-ESAC, 2005, http://www-panda.gsi.de.

[11] T. Mersmann *et al.*, Phys. Rev. Lett. **98** (2007) 242301.

[12] J. Smyrski *et al.*, Phys. Lett. **B 649** (2007) 25898.

[13] N. Hamann *et al.*, *First Antiproton Interactions with the Hydrogen-Cluster Jet Target at LEAR*, First Biennial Conference on Low Energy Antiproton Physics, Stockholm, Sweden, eds.: P. Carlson, A. Kerek and S. Szilagy, World Scientific, 1991, p. 231.

[14] A. Täschner *et al.*, annual report 2006, Forschungszentrum Jülich, JÜL-4234, p. 48

5 Pellet Target

5.1 Introduction

Pioneering work on pellet targets was made at Uppsala University and at the TSL, Uppsala. This has resulted in an operational system for the WASA detector facility which is now being used at COSY-Jülich. However, further developments are necessary to meet specific requirements in connection with high-luminosity experiments at HESR. For example, the pellet generator has to be located outside the PANDA detection system, *i.e.* significantly further away from the interaction zone as compared to WASA.

This puts stringent demands on the divergence and steadiness of the pellet stream. The size and rate of the pellets should be optimized for HESR operation, *i.e.* the pellet size should be reduced to $10\,\mu m$ or less and the pellet rate increased as much as possible, keeping an effective target thickness of the order of a few times 10^{15} atoms/cm^2. The aim is to always have one, and only one, pellet intercepting the circulating beam.

Central part of a pellet target is the triple-point chamber (TPC). In that chamber a jet of a cryogenic liquid is injected through a thin nozzle (with diameter roughly equal to the pellet diameter) into the same gaseous material close to triple-point conditions. Periodic excitation of the nozzle by a piezoelectric transducer imposes jet oscillations along its surface. The axially symmetric jet then disintegrates into drops downstream the nozzle when the perturbation amplitude becomes equal to the jet radius. From the TPC — which makes sure that an extremely regular drop flow can be produced under optimal conditions without disturbances from evaporation [1] — the drops pass through a thin tube into vacuum. During that transition they cool, due to surface evaporation, by a few Kelvin below the melting point, and a regular flux of very stable frozen pellets is produced.

Key issues for the improvement of pellet generators are:

- Unwanted vibrations of the jet-producing nozzle must be suppressed in order to allow for satellite-free and mono-disperse drop formation [1].
- The generator must be operated in a wide temperature range in order to allow pellet production from different cryogenic liquids.
- The geometry of the transition unit between TPC and vacuum must be such that turbulences in the rapidly flowing gas inside are minimized (and, thus, distortions of the produced pellets).

Such a new generation of pellet targets has been developed by a joint effort of the Forschungszentrum Jülich (FZJ), the Institute of Theoretical and Experimental Physics (ITEP) and the Moscow Power Engineering Institute (MPEI). Due to a novel and patented [2] cooling technique and a careful optimization of drop-production processes, the targets provide extremely regular pellet beams.

5.2 The Moscow-Jülich Pellet Target

The groups from FZJ, ITEP and MPEI have built three pellet generators [3, 4]:

1. The generator at FZJ is the most advanced one. It comprises a cryostat with baths of liquid N_2 and He (see Fig. 5.1). Liquefaction of H_2 is achieved in three stages: first cooling with liquid N_2, further cooling in a heat exchanger by evaporated He, and final cooling in the condenser by cold He gas. From the condenser, the liquid passes through the vibrating nozzle and reaches the TPC.
2. The target at ITEP has a simpler cooling scheme (only one stage) and allows one to study jet and pellet production from N_2, Ne, Ar, Kr and Xe.
3. The MPEI drop generator is without cooling and is used for developing the diagnostic system that measures drop and pellet parameters. It also allows one to test and develop models on water drop production.

In brief, the results of the developments at FZJ/ITEP/MPEI are:

- A patented [2] vibration-less cooling technique which provides “ideal” jets of cryogenic liquids

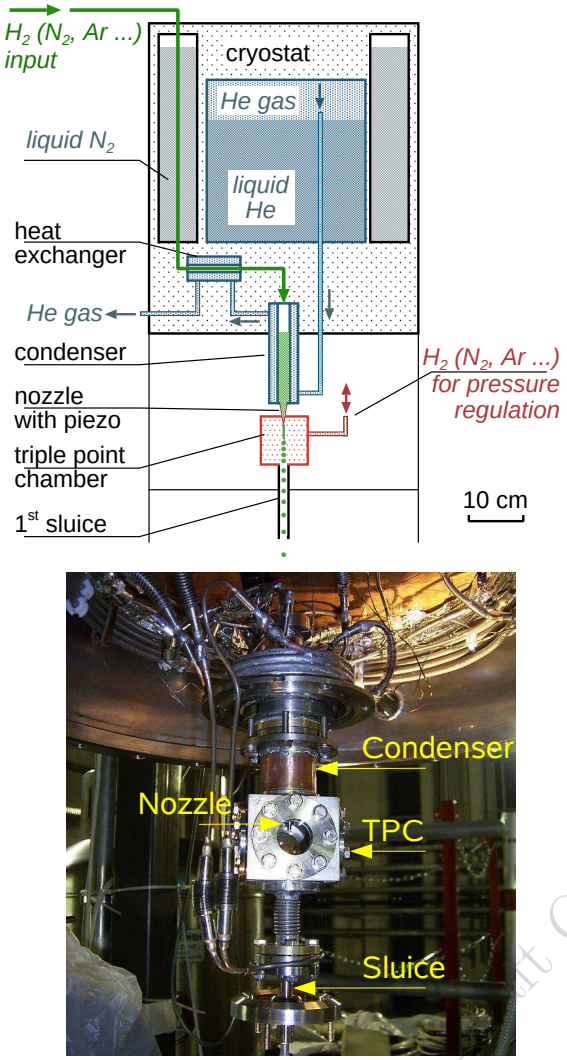

Figure 5.1: Sketch and photo (central part) of the FZJ pellet generator. The cryostat (total height ∼0.8 m, not drawn to scale) comprises the cooling liquids (N_2 and He) as well as the heat exchanger and the upper part of the condenser. The condenser houses a few cm^3 of the cryogenic liquid which is driven through a nozzle into the TPC by overpressure. Constant pressure in the TPC is maintained by an auxiliary gas feeding.

has been developed. This allows one to produce mono-disperse drop fluxes with minimum divergence.

- The working parameters for the satellite-free and mono-disperse jet breakup have been established (see Fig. 5.2 and Table 5.1 for examples).

- The drop generator can be operated with various cryogenic liquids, like H_2, D_2, N_2, Ar, Kr and Xe. Stable pellet production has so far been observed for H_2, N_2 and Ar.

- The transition unit ("sluice") between TPC and vacuum has a circular cross section with a radius that decreases exponentially to in flight direction.

5.2.1 Performance of the Prototype Pellet Generator

During test measurements two different nozzle types have been utilized, glass nozzles in brass housings and such made from stainless steel. The former, with inner diameters of 12–30 μm at the nozzle tip, have the advantage of a smooth internal surface and allow one to look inside the channel during operation. The 16–30 μm steel nozzles offer high shape reproducibility and smaller length-to-diameter ratios of the holes, allowing operation with lower jet-driving pressures. The results shown here have been obtained with glass nozzles and pressures of ∼0.4–0.9 bar for H_2 and ∼1.0–1.5 bar for N_2; higher pressures lead to higher jet velocities. The piezo-electric transducer allows one to excite sinusoidal nozzle vibrations in the range f=1–100 kHz.

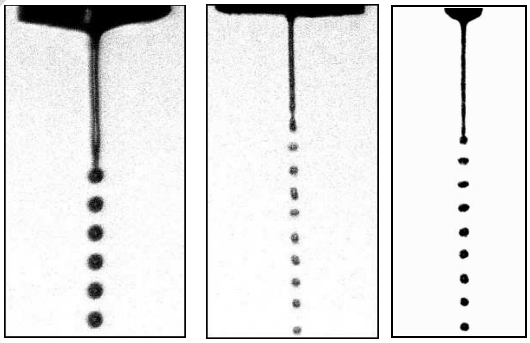

Figure 5.2: First observation of satellite-free and monodisperse disintegration of N_2 (left), H_2 (middle) and Ar (right) jets. In the upper edge of the photos the tip of the vibrating nozzle can be seen.

Figure 5.2 shows the breakup of N_2, H_2 and Ar jets in the TPC; for certain choices of the jet and TPC parameters (see Table 5.1 and Ref. [1] for details), stable satellite-free and mono-disperse drop production has been achieved.

When the drops leave the TPC through a 1st sluice into a subsequent chamber (p=$o(10^{-2})$ mbar), they freeze to pellets due to strong surface evaporation, and are accelerated by the gas flow from the TPC. Then the pellets pass a 2nd sluice and a 2nd chamber

Table 5.1: Parameters of the H_2 and N_2 jets from Fig. 5.2.

	N_2	H_2
TPC pressure (mbar)	300	130
TPC temperature (K)	74	17
Jet temperature (K)	77.2–77.0	20.0–19.8
Nozzle frequency f (kHz)	26	38
Jet diameter $2R_0$ (μm)	17	12
Jet velocity $v_{\rm jet}$ (m/s)	2.6	2.4
Initial perturbation δ	0.02	0.02
Jet length (μm)	310	290

($o(10^{-4})$ mbar), and finally reach a dummy scattering chamber through a thin tube ($\varnothing \sim 2$ cm), which is currently located 1.2 m downstream of the TPC. In order to minimize turbulences of the gas flow in the 1st sluice it has a circular cross section with a radius that decreases exponentially to 600 μm in flight direction. For pellet observation two CCD cameras have been positioned at the outlet of the 1st sluice or at the dummy chamber.

So far, stable H_2 and N_2 pellet production with diameters 20–40 μm (the pellet diameter is about two nozzle diameters), and a pellet rate of a few 10 kHz has been observed. Deviations from the mean pellet diameter are below 1% (10%) over periods of few seconds (hours). The average velocity of 30 μm pellets amounts to ~70 m/s, see Fig. 5.3. The radial displacement of the pellets from their nominal flight path in a dummy chamber (at a distance of more than one meter from the drop generator) of about $\pm 200\,\mu$m has been extrapolated from the angular pellet distributions measured behind the 1st sluice. This value is dominated by the experimental resolution.

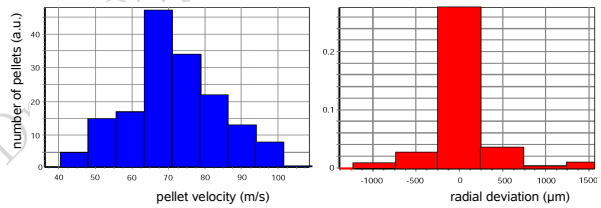

Figure 5.3: Velocity and spatial distributions of H_2 pellets in the scattering chamber.

From the jet and drop parameters in the TPC together with the measured pellet velocity, the pellet-to-pellet distance in the scattering chamber can be calculated (assuming that all drops reach the chamber as pellets). For the H_2 jet from Fig. 5.2 and Table 5.1 one obtains a value of 1.65 μm which will be experimentally verified during future tests at FZJ.

Based on the layout and experience of the prototype pellet generator the PANDA pellet target will be built. This new target will comprise a new adjustment system for the vibrating nozzle which will be installed and tested in 2009. This system must be able to align the nozzle axis with that of the transition tube into the vacuum, at room temperature (for pre-adjustment) and at liquid-Helium temperature (fine adjustment during operation).

5.3 Target Infrastructure

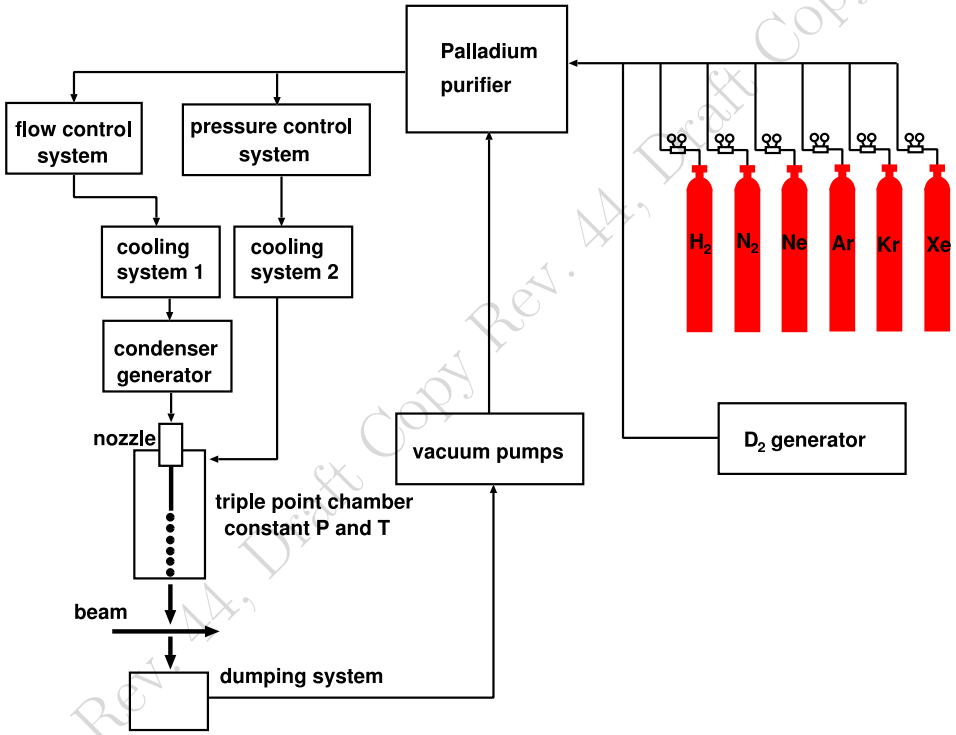

Figure 5.4: Schematic drawing of a gas supply system for the pellet source.

5.4 Time Schedule

Work package	***Year***								
	2007	2008	2009	2010	2011	2012	2013	2014	2015
R & D with prototypes at FZJ, MPEI and ITEP									
Preparation of test stands for PANDA target									
Construction of: Pellet generator									
Vacuum system									
H_2, He and N_2 supply systems									
Adjustment systems									
Installation & tests in Russia									
Transfer to FAIR									
Installation at FAIR									
Adjustment and tests without beam									

Figure 5.5: Time schedule for the implementation of the pellet generator.

Bibliography

[1] A. V. Boukharov *et al.*, Phys. Rev. Lett. **100** (2008) 174505 [arXiv:0804.1782 [physics.flu-dyn]].

[2] A.V. Boukharov, M. Büscher, *Verfahren und Vorrichtung zur Kühlung eines Gases*; German Patent Application No. 10 2007 017 212.7-13 and Russian Federation Patent No. 2298890, Worldwide PCT application in preparation.

[3] A. Boukharov, V. Chernetsky, A. Dmitriev, V. Chernyshev, *"Pellet target for experiments on internal beam of accelerators"*, 13$^{\text{th}}$ Annual Conference of Liquid Atomization and Spray Systems, July 9–11 1997, Florence, Italy.

[4] M. Büscher, P. Fedorets, V. Chernetsky, V. Chernyshev, A. Bukharov and A. Semenov, "The Moscow-Jülich frozen-pellet target," AIP Conf. Proc. **814**, 614 (2006).

6 Beam Target Interaction

COMMENT: Author: D. Prasuhn, H. Orth, M. Büscher, A. Khoukaz

6.1 Beam Requirements for Different Target Types

6.2 Beam Life Times

6.3 Time Structure of the Luminosity

6.4 Effective Luminosities

7 Target Beam Dump

COMMENT: Author: A. Bersani, H. Orth, A. Khoukaz, H. Calen

The target material, either the solid hydrogen pellets or the hydrogen cluster stream, crosses the whole Target Spectrometer and is collected in a sink. The Target Beam Dump has been optimised to be compatible, with minor modifications, for both the pellet and cluster jet targets.

The concept of the Target Beam Dump is essentially symmetric to the target production stage. The cluster or pellet stream collides to a kind of "collector" and the beam pipe vacuum is protected by a multi-stage differential pumping system. The collector is a trap for the pellets and a turbomolecular pump for the clusters. The differential pumping system is all equipped with turbomolecular pumps. A proper forevacuum system has been designed to allow the best vacuum performances. Several diagnostic devices, especially for the pellet target, are integrated in the Target Beam Dump.

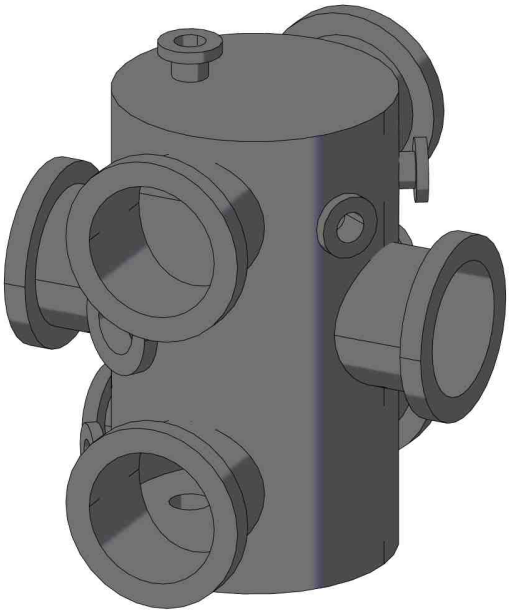

Figure 7.1: View of the target dump vacuum chamber. The hydrogen jet enters through the upper flange and gets out through the lower hole (visible through the lateral lower flange). All the flanges both for pumps and diagnostics are shown.

7.1 Differential Pumping System

The differential pumping system that will be used in the $\overline{\text{P}}$ANDA experiment is based on the vacuum chamber which was built for the JETSET (PS202) [1] experiment at CERN. The JETSET experiment was installed on the LEAR antiproton ring, and featured an internal cluster jet target with a free flight between the production and the dump of $\sim$ 2 m. The core of this Target Beam Dump is a three-stages differential pumping system.

The vacuum chamber features two internal walls, with two holes, through which the target material can pass. The beam does not cross the vacuum chamber on its axis, but at 75 mm from it. This has been designed for the cluster jet target: the stream collides on the blades of a turbomolecular pump that is installed under the vacuum chamber, centred on its axis. This causes the largest part of the hydrogen to be evacuated directly through that pump, greatly reducing the gas back-flow to the beam pipe. Each stage is equipped with two CF150 flanges to which two turbomolecular pumps can be attached. A view of the vacuum chamber is shown in Fig. 7.1.

The different stages will be connected with conical pipes to further reduce the gas flow from the dump to the beam pipe. The shape and length of these pipes has been optimised to have the best insulation between the stages. A cross section of the vacuum chamber, showing these pipes, is reported in Fig. 7.2

We foresee to use two turbomolecular pumps for each stage, both for the cluster jet target and for the pellet target operations. We foresee to use two VARIAN Turbo-V 551 Navigator in the first stage and four VARIAN Turbo-V 1001 Navigator in the second and third stages [2]. The use of smaller pumps in the first stage is due to space considerations; on the other hand, we expect the lowest gas load in the first stage, so the lower pumping speed will not affect the operations. The VARIAN Turbo-V 551 Navigator features a CF150 flange, so can be attached directly to the vacuum chamber, whereas the VARIAN Turbo-V 1001 Navigator features a CF200 flange, so it is attached to the vacuum chamber through a zero-length transition.

The choice of this model of turbomolecular pumps was driven by the need of a high pumping speed

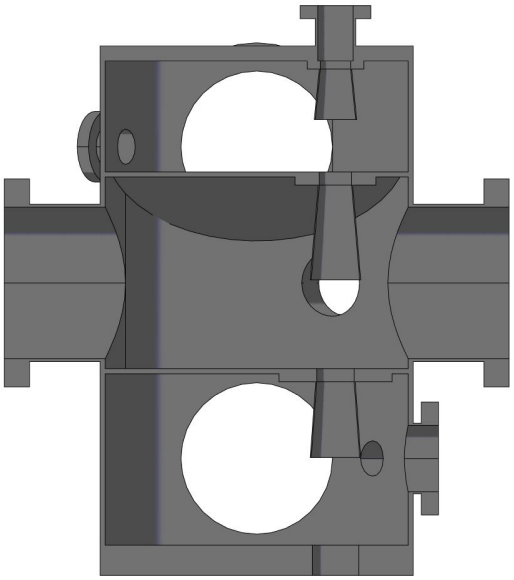

Figure 7.2: Section of the target dump vacuum chamber. The conical pipes designed to reduce the gas backflow are visible on the right side.

for hydrogen, even at relatively high pressure. The VARIAN turbomolecular pumps feature a first stage, based on molecular impellers, which ensures full pumping speed up to 10^{-3} mbar in the inlet, decreasing to 90% of the maximum at 10^{-2} mbar for the chose pump models. A summary of the pumps performances is reported in Table 7.1.

Table 7.1: VARIAN turbomolecular pumps parameters.

	551	1001
Pumping speed	510 l/s	900 l/s
Compression ratio	10^6	10^6
Max. foreline pressure	~ 5 mbar	~ 10 mbar

The expected performances of the 1001 Navigator pumps are, anyhow, under the reported values due to the introduction of the zero-length transition, which reduces the conductance to the pumps blades. According to the specifications of the manufacturer, we expect a effective pumping speed $\sim 5\%$ lower than the nominal one.

Each stage of the Target Dump will be equipped with Leybold ITR90 [3] pressure gauges, to continuously monitor the pressure profile and the gas backstream. An additional low-vacuum Pirani gauge will be mounted in the last stage for monitoring during the evacuation and vacuum breaking.

7.2 Pellet Tracker

A system to monitor the pellet stream parameters will be mounted on top of the Target Beam Dump.

7.3 Cluster Set-Up and Performances

The Target beam Dump, to be operated with the cluster jet generator, will be equipped with a VARIAN Turbo-V 1001 turbomolecular pump, on the bottom side. Since the cluster jet travels ~ 75 mm far from the vacuum chamber axis, it will arrive directly on the blades of the turbomolecular pump. There it will be destroyed and efficiently pumped away.

7.4 Pellet Pot

To be operated in conjunction with the pellet generator, the turbomolecular pump on which the target material arrives will be removed and replaced by a properly designed pellet trap.

7.5 Forevacuum System

A properly designed forevacuum system provides evacuation to the target dump down to a fraction of millibar.

7.6 Installation and Maintenance

Bibliography

[1] T. Ander *et al.*, Nucl. Phys. Proc. Suppl. **8** (1989) 69.

[2] Varian, Inc. website and catalogues therein, http://www.varianinc.com

[3] Oerlikon Leybold Vacuum GmbH website and catalogues therein, http://www.oerlikon.com/leyboldvacuum

8 Vacuum System

COMMENT: Author: D. Prasuhn, J. Zmeskal

FOR THE TIME BEING JUST COPY/PASTE FROM TPR:

8.1 Vacuum System and Tubing

The vacuum system has to fulfill several requirements. First of all, the vacuum system has to warrant the optimal operation of all vacuum stages of the structural components. Secondly, the gas flow originating from the target installation to the vacuum stages of the accelerator beam line must not exceed a certain limit. This limit itself depends on the pumping speed at the target and at the beam line close to the interaction region, the conductance of vacuum pipes connecting these pumps with the vacuum system as well as on the target thickness itself. Furthermore, regeneration intervals in the case of using cryopumps as well as sensitivity to magnetic fields have to be taken into account.

concerning target-common:

An approved method to evacuate this stage is to use a special designed cryopump (TPR-Fig. 4.23). This pump combines pump and vacuum stage in one unit and allows for maximum pumping capacities for the reduction of residual gas.

Due to the small diameters of the apertures in the cluster source the cryopump will be connected to the collimator stage by a vacuum pipe and a valve for regeneration. This type of connection can be omitted at the larger apertures in the cluster beam dump.

8.2 Pumping Scheme

An internal target system necessitates a sufficient pumping system as close to the interaction zone as affordable, to keep the beam vacuum below 10^{-7} mbar. Conventional pumping systems, such as turbo molecular pumps and ion getter pumps, cannot be installed due to stringent requirements to the available space around the interaction zone. The space is occupied by the necessary detector systems, as is clearly seen in Fig. *(TPR-4.43 - here new cut of TS will be made from the vacuum design by AG)*. Therefore, it is proposed to use the walls of the beam pipe inside the detector as well as the internal target vacuum pipe itself as a high-vacuum pump. This could be achieved by coating the surface with a non-evaporable getter (NEG) material as is used at CERN for the LHC. Additional pumping is necessary as sketched in Fig. *(TPR-4.44 - here new cut of full detector will be made from the vacuum design by AG)*. Two turbo-molecular pumps, each with a nominal pumping speed of 1 000 l/s, will be installed in front of the PANDA magnet. A specially designed cryo-sorption pump (with an additional pumping speed of 5 000 l/s) will be used *(is this still valid?)*. Two additional turbo-molecular pumps (each 500 l/s) will be located further away from the beam pipe, in-between the PANDA magnet and the forward spectrometer. Another turbo-molecular pump (1 000 l/s) and an ion getter pump (800 l/s) at the end of the forward spectrometer will complete the beam line pumping system (see Fig. TPR-4.44). A detailed study of gas losses in the interaction region for cluster-jet and pellet targets is under evaluation. A prototype vacuum chamber is set up at SMI with NEG coated walls. It has the foreseen effective pumping speed as it would be available with the pumping equipment and dimensions of the beam pipes as shown in Figs. (TPR-4.44 4.45). Different gas loads (hydrogen gas lost in the interaction zone either coming from the cluster-jet or pellet beam) will be measured and compared with the theoretical calculations.

8.3 NEG

Non-evaporable getters remain in the solid state instead of being evaporated and condensed on a surface (as with Ti-sublimation pumps). This family of getters is usually made of an alloy of zirconium, such as Zr-Al, Zr-V-Fe or Zr-V-Ti. Although they can exist in any solid form, they are most often found as either chunks or pellets or thin films bonded to metallic substrates. NEGs are known for their high pumping speed and capacity for hydrogen. Further advantages are the relatively small size and little weight. An activation process is required for NEGs. When the getter material is exposed to air for handling or loading into a system or device, the materials surface will skin over with reacted gases. This means that the NEG will be entirely enclosed in an envelope of oxides or nitrides.

Additionally, the bulk of the material will encompass dissolved H_2. Under these conditions, the getter material is essentially inert and will not provide an active getter pumping surface. Activation prepares the getter surface for pumping and is performed by heating under vacuum after installation. During heating, the reacted skin layer will diffuse into the NEGs bulk in an attempt to achieve equilibrium throughout the bulk. The H_2 will be driven out of solid solution into the chamber and pumped away by an appropriate high-vacuum pump. The time and temperature required for activation will vary with the specific getter alloy. The vacuum level required will depend upon the actual application, but a pressure of at least 10^{-6} mbar is usually required. The pumping time must be sufficiently long to ensure that the released H_2 is pumped away. Any remaining H_2 will be reabsorbed by the getter and this will limit the amount of H_2 subsequently pumped by the getter. After activation, gases will be removed from the vessel by reaction on the NEGs surface until enough gas is reacted to put a gas layer over the surface again (skin over). At this point, pumping action for active gases ceases and the reacted skin becomes a barrier for further dissolution of H_2. The time required for this to happen is a function of the gas load to be pumped. In ultrahigh-vacuum applications, it can be in the order of years. However, in an environment with high gas loads the time could be reduced to hours or minutes. Gas loads that result in an unacceptably short period of surface saturation are usually dealt with by raising the temperature of the NEG to a about 80 to 100℃. The higher temperature will result in pumping and diffusion into the bulk taking place at the same time. Systems which are cycled repeatedly to atmospheric pressure require careful consideration. Each time the NEG material is in contact with air or any other active gas, such as N_2, re-activation is required. In a cycled system, the chamber can be released to argon instead of an active gas or the getter can be isolated from the chamber by appropriate valves. Getters and getter pumps can provide economical and compact pumping in many applications if they are used properly. Vacuum pumping via non-evaporable getter thin film deposited directly onto the interior of a vacuum chamber is a novel way to produce high vacuum.

The performance of a NEG is characterized by activation temperature, sticking probability, surface capacity and total pumping capacity. For the study of a thin film NEG coated vacuum chamber, having similar dimensions as it will be used at the interaction zone (see Fig. TPR-4.44), a prototype was set up to measure

- gas load,
- pumping speed
- recycling time

for a realistic assumption of hydrogen gas losses using an internal target device.

9 Gas Supply System

COMMENT: Author: J. Zmeskal

9.1 Gas Purifier

FOR THE TIME BEING JUST COPY/PASTE FROM TPR:

A schematic drawing of the gas supply system for the cluster-jet target at PANDA is presented in Fig. 4.5. The target device has to be operated with H_2 gas with as high a purity as possible to avoid blocking of the cryogenic nozzle by impurities like O_2 or N_2 when operated at temperatures below 30 K. For this purpose, H_2 of standard purity (e.g. 99.999%) will be fed to the gas supply system. The gas is cleaned by a purifier with a heated palladium membrane to optimize the purity (i.e. no impurities detectable). For technical reasons, this device has to be operated with N_2 in parallel. However, N_2 cannot pass the Pd membrane. For security reasons, both the N_2 and H_2 gas bottles have to be placed in a special gas cabinet. The size of this gas cabinet should be sufficiently large to contain at least four hydrogen bottles (50 l, 200 bar) and one nitrogen bottle in parallel. After the purification stage the gas will be led through a gas flow monitor and control system and enters the cluster source unit. At this stage, a micrometer filter is included into the gas feeding system to efficiently remove micro-particles. Finally, the gas passes the cooling stages of the cryogenic cold head and enters the nozzle. A Baratron capacitance manometer is connected to the gas system parallel to the nozzle in order to monitor the gas pressure directly before passing the nozzle.

9.2 Deuterium Recuperation

If longer periods with deuterium cluster beams are planned, the gas supply system can be enlarged by a D_2 recuperation system as it is used with the targets at COSY. This system collects the D_2 gas exhausted by the vacuum pumps at the cluster-jet source and supplies it to an oil-free compressor which finally provides the D_2 gas with a pressure of 20 bar. For a further reduction of the operational cost, a D_2 generator can be used which generates D_2 gas from liquid D_2O with a sufficient quality to feed the palladium purifier of the target installation. Such a system is currently being tested at the experiment ANKE at COSY.

10 Slow Control System

COMMENT: Author: A. Bersani, H. Orth only requirements and two possible solutions (Labview, Simatic)

11 Infrastructure

COMMENT: Authors: H. Orth, D. Prasuhn
here we should specify what we need and what we consume...

11.1 Power Supply

11.2 Cooling Liquids

11.3 Compressed Air

11.4 Pump Exhaust

11.5 Required Testing Areas

We need place for testing, repairing, optimization, the targets transported to FAIR. This area should be accessible during beam times.

12 Timelines

COMMENT: Author: A. Khoukaz, H. Orth

The timelines are driven in part by the envisaged start of commissioning of HESR early in 2014. In particular, the vacuum pipe system inside the solenoidal magnet needs to be in place in order to allow any beam operation. For the commissioning phase of $\overline{\text{P}}$ANDA as well as for the first experimental program it is proposed to start with the cluster jet target since only this target system allows for a continuous variation of the target density over orders of magnitude. Especially during the first operation of the $\overline{\text{P}}$ANDA detector this will allow to test all components starting with low event rates, which can then be increased continuously. Similarly, the commissioning of the beam cooling systems foreseen at HESR can be performed well with a cluster beam adjusted in the beginning to low areal beam densities.

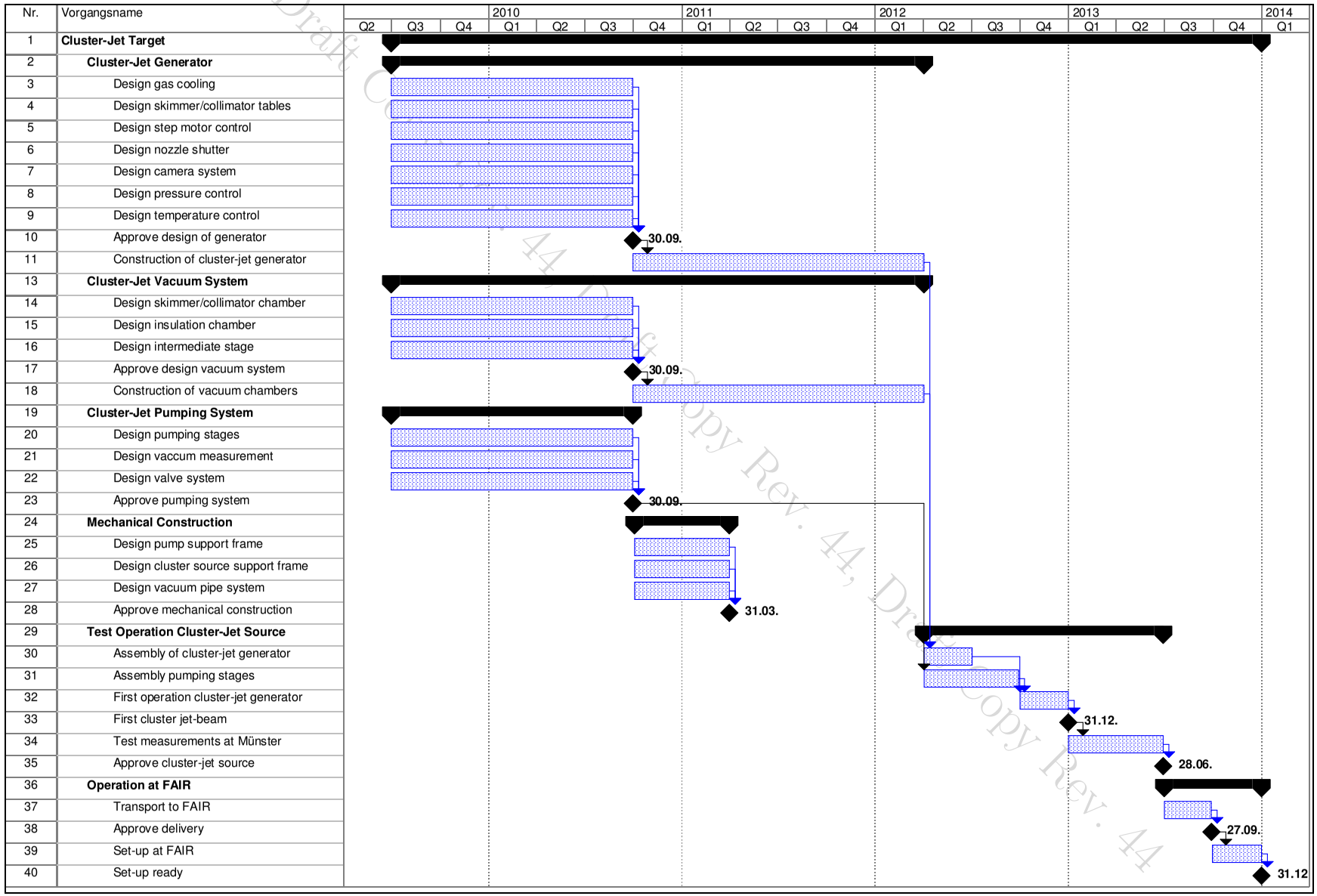

Figure 12.1: Timelines for the cluster jet target.

13 Appendices

List of Figures

List of Tables